Received: 27 April 2021 | Revised: 24 February 2022 | Accepted: 7 March 2022

DOI: 10.1111/gbi.12492

ORIGINAL ARTICLE

gebiology WILEY

Microbially promoted calcite precipitation in the pelagic redoxcline: Elucidating the formation of the turbid layer

Kerstin M. Leberecht[1] | **Simon M. Ritter**[2] | **Christian J. Lapp**[1] | **Lukas Klose**[3] | **Julian Eschenröder**[2] | **Christian Scholz**[2] | **Sebastian Kühnel**[2] | **Wolfgang Stinnesbeck**[2,4] | **Arnulf Kletzin**[5] | **Margot Isenbeck-Schröter**[2,4] | **Johannes Gescher**[1]

[1]Institute of Technical Microbiology, Hamburg University of Technology, Hamburg, Germany

[2]Institute of Earth Sciences, Heidelberg University, Heidelberg, Germany

[3]Department of Physics & Earth Sciences, Jacobs University Bremen, Bremen, Germany

[4]Heidelberg Center for the Environment (HCE), Heidelberg University, Heidelberg, Germany

[5]Department of Biology, Microbiology; Sulfur Biochemistry and Microbial Bioenergetics, Technical University of Darmstadt, Darmstadt, Germany

Correspondence

Johannes Gescher, Institute of Technical Microbiology, Hamburg University of Technology (TUHH), Kasernenstraße 12, Hamburg 21073, Germany.

Email: johannes.gescher@tuhh.de

Funding information

Deutsche Forschungsgemeinschaft, Grant/Award Number: STI128/28 and STI128/36; CONACYT-FONCICYT-DADC, Grant/Award Number: 000000000278227

Abstract

Large bell-shaped calcite formations called "Hells Bells" were discovered underwater in the stratified cenote El Zapote on the Yucatán Peninsula, Mexico. Together with these extraordinary speleothems, divers found a white, cloudy turbid layer into which some Hells Bells partially extend. Here, we address the central question if the formation of the turbid layer could be based on microbial activity, more specifically, on microbially induced calcite precipitation. Metagenomic and metatranscriptomic profiling of the microbial community in the turbid layer, which overlaps with the pelagic redoxcline in the cenote, revealed chemolithoautotrophic Hydrogenophilales and unclassified β-Proteobacteria as the metabolic key players. Bioinformatic and hydrogeochemical data suggest chemolithoautotrophic oxidation of sulfide to zero-valent sulfur catalyzed by denitrifying organisms due to oxygen deficiency. Incomplete sulfide oxidation via nitrate reduction and chemolithoautotrophy are both proton-consuming processes, which increase the pH in the redoxcline favoring authigenic calcite precipitation and may contribute to Hells Bells growth. The observed mechanism of microbially induced calcite precipitation is potentially applicable to many other stagnant sulfate-rich water bodies.

KEYWORDS

biogeochemistry, chemolithoautotrophy, microbially induced calcite precipitation, redoxcline, sulfide oxidation

1 | INTRODUCTION

Microbially induced calcium carbonate precipitation (MICCP) is an example for the potential effects of microbial metabolic activity on geochemistry (Görgen et al., 2020). The results of this process are widely distributed in nature and can be found in diverse environments (Dupraz et al., 2009). Large bell-shaped calcite structures were discovered underwater by cave divers in the cenote El Zapote (20°51′13.8″N 87°07′31.2″W; Figure S1) on the Yucatán Península, Mexico (cenote, local term for sinkhole; Figure 1). They termed these extraordinary structures as Hells Bells due to their appearance in darkness and the vicinity to a sulfidic halocline. Hells Bells are characterized by their bell- or cone-like shape and downward extension with a hollow interior reaching sizes of up to ~4 m. Hells Bells are built up by alternating layers of micritic and sparry or dog-tooth-like calcites with crystal sizes of up to several mm, which indicate inorganic precipitation (López-Martínez et al., 2020; Ritter et al., 2019; Stinnesbeck et al., 2018). They apparently grow underwater (Stinnesbeck et al., 2018) in an otherwise carbonate dissolving karstic aquifer environment, where the water masses are generally only saturated or even undersaturated with respect to calcite. In karstic settings, calcite precipitation usually occurs due to CO_2-degassing in areas where water is in contact with the atmosphere, for example, dripstone formation in caves (Huggett, 2003) or calcite raft formation at the water surface of subsurface cenotes and caves (e.g. Kovacs et al., 2017). This raises many questions regarding the processes leading to the subaqueous formation of Hells Bells. Lately, Hells Bells formation was suggested to initially result from CO_2-degassing of ascending gas bubbles that accumulate at cave irregularities and further growth of these structures in the carbonate-saturated freshwater layer of cenote El Zapote (López-Martínez et al., 2020). However, this hypothesis is solely based on the

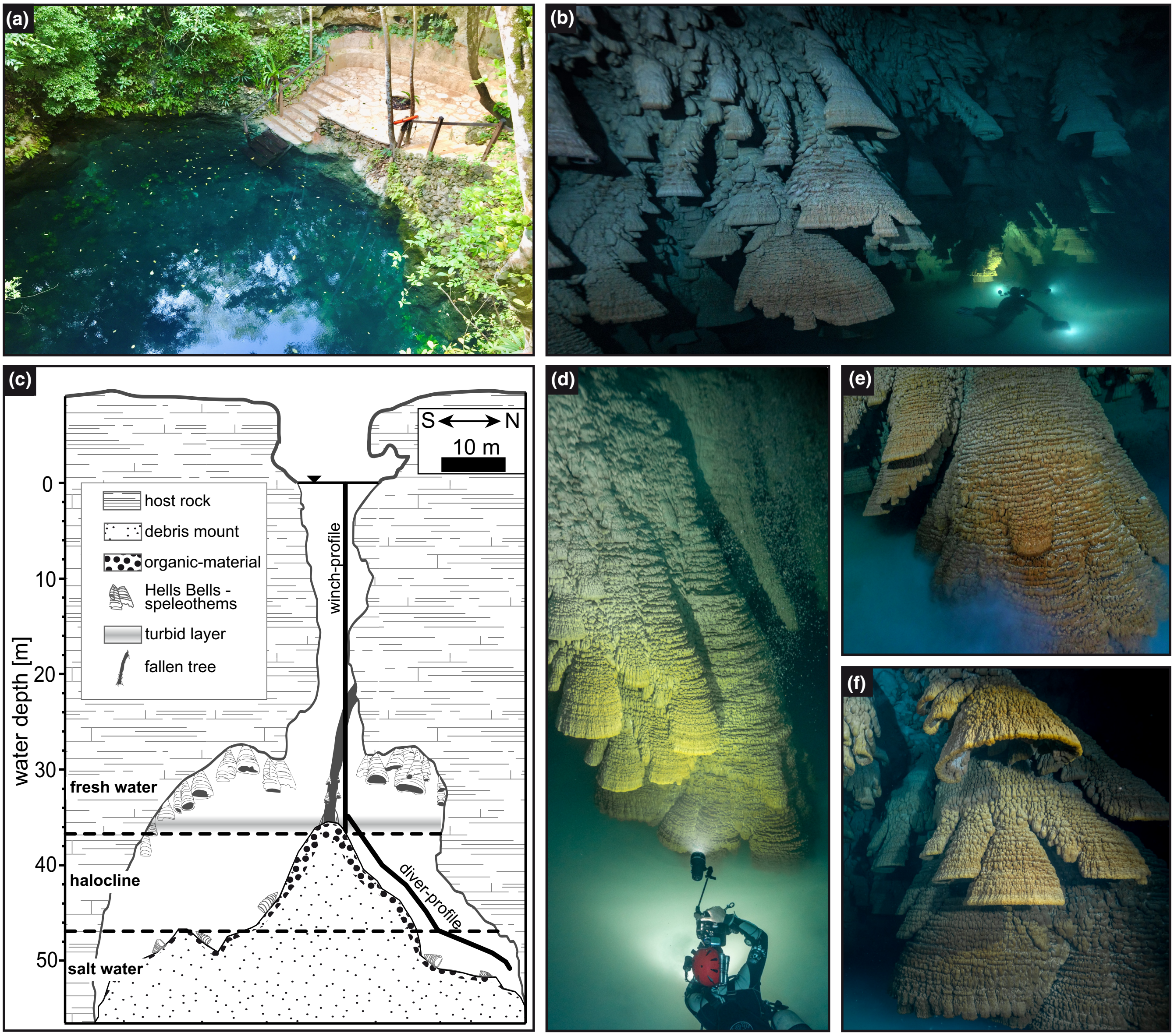

FIGURE 1 Cenote El Zapote hosts extraordinary bell-shaped calcite formations. (a) View on the cenote water surface from above. (b) Hells Bells speleothems growing down the ceiling and inclined walls of the cenote. They can reach a size of ~4 m. (c) Schematic cross section of cenote El Zapote. Hells Bells speleothems cover the cave ceiling and wall in a freshwater zone above the anoxic, sulfidic halocline in water depths of 28–38 m. (d) Technical diver studying Hells Bells speleothems above the turbid layer. (e) A large specimen of a Hells Bells speleothem that reaches into the white, cloudy turbid layer, the water zone in which Hells Bells grow. (f) Hells Bells speleothems are characterized by a bell-like downward extension with a hollow interior. They show a horizontal growth pattern in form of horizontal laminations and swellings. Photographs (b, d–f) by Valentina Cucchiara (Liquid Jungle Media, Playa del Carmen, Mexico; 2020)

observation of structures in the cave ceiling that were interpreted as bubble trails. Prior to that, Ritter et al. (2019) reported detailed hydrogeochemical profiles, chemical and optical analyses on Hells Bells carbonate speleothems and SEM analyses on filtrates of the turbid layer of El Zapote. They showed that Hells Bells most likely grow in the lowermost freshwater body as indicated by uranium isotopes of Hells Bells carbonate samples and the comparison of Mg/Ca ratios of the water body and Hells Bells carbonates. Accordingly, the actual growth of Hells Bells is most likely restricted to the pelagic redoxcline, a 1–2-m-thick intermediate zone of steep redox gradients of electron acceptors and reduced chemical species above a sulfidic halocline. The redoxcline overlaps with a distinct milky, white horizontal cloud, the turbid layer, into which some Hells Bells partly reach or hang completely inside (Figure 1b–e). Based on these results, a biologically induced authigenic calcite precipitation within the turbid layer was hypothesized (Ritter et al., 2019). This would imply a chemolithoautotrophic community that promotes basification via CO_2 fixation and the catalysis of a nitrate-dependent incomplete sulfide oxidation to zero-valent sulfur. The permanent fixation of this calcite in Hells Bells over a wide vertical range of ~10 m water depth might be the result of a variable elevation of the halocline and with it the redoxcline and thus the zone of calcite precipitation (Ritter, 2020; Ritter et al., 2019). Also, such a repeated elevation of the calcite dissolving halocline could explain the observed internal layered structure of Hells Bells speleothems, which most likely represents repeated phases of calcite growth and dissolution. The halocline elevation might vary on both, long and short time scales due to changes in sea level over glacial periods over tens of thousands of years, extended droughts over hundreds of years, annual tidal variations, seasonal variations of the thickness of the freshwater layer over months, and short-term aquifer responses on heavy precipitation events over days and weeks. Furthermore, age-dating of Hells Bells specimens from different water depths indicated varying growth rates over time, which might be related to variations of the halocline position on centennial–millennial scale (Ritter, 2020).

Nitrate-driven sulfide oxidation was reported before in the context of calcite precipitation in sediments (Bailey et al., 2009; Himmler et al., 2018), in which microorganisms thrive in gradients of sulfide as electron donor and nitrate as electron acceptor. Here, precipitation is based on a combined effect of the dissimilatory reduction of nitrate, sulfide oxidation, and anaerobic sulfate-driven methane oxidation. In contrary, the here described ecosystem is comprised of a very different microbiology that catalyzes an incomplete oxidation of sulfide coupled to denitrification.

In this study, we elucidated how a complex interaction of chemolithoautotrophic microorganisms catalyzing reactions of the sulfur and nitrogen cycle could induce local calcite precipitation within the pelagic redoxcline forming a distinct turbid layer. Taxonomic and functional profiling combined with high-resolution *in situ* parameters revealed strong geochemical and biological evidence that microbial metabolic activity in the planktonic phase promotes authigenic calcite precipitation in the redoxcline by increasing the local pH through the depletion of sulfide, nitrate, and carbon dioxide.

2 | MATERIALS AND METHODS

2.1 | Site description

The cenote El Zapote is localized to the southeastern part of Mexico on the Yucatán Peninsula in the federal state of Quintana Roo (20°51′13.8″N 87°07′31.2″W; Figure S1). The vertical profile of El Zapote shows that the cenote has a bottle-like shape with a narrow shaft that reaches from the water surface to a water depth of 28 m, which then turns into a dome-like contour (diameter: 60–100 m; Figure 1). The cenote has a maximum depth of about 54 m, however, in the center there is a debris mound that reaches a water depth of about 36 m. Right on the peak of the debris mound, a fallen tree was found that shows small Hells Bells grown on the stem surface. A high-resolution 3D model of the cenote walls including the Hells Bells speleothems is available on https://doi.org/10.11588/heidicon/1264341 and illustrates the complexity of the underwater cave. For a more detailed description of El Zapote, see Stinnesbeck et al. (2018).

2.2 | Water sampling and on-site measurements

Sampling at the cenote El Zapote was carried out during the period from May 31 to June 6, 2018. The *in situ* parameters pH (±0.1; relative accuracy ±0.01), EH (±20 mV), dissolved oxygen (±0.1 mg L^{-1}, detection limit 0.1 mg L^{-1}), electrical conductivity (±0.05% of value), temperature (±0.01 °C), and turbidity (±2% of value) were determined with the multiparameter sonde EXO 1 (Xylem Analytics, Norway). All parameters, including the water depth via pressure measurement, were internally logged by the sonde (±0.04 m). Water depths were corrected to the ambient air pressure and to the increasing salinity below a water depth of 36 m (Ritter, 2020). Multiple winch-operated profiles of *in situ* parameters were conducted from the surface to the top of the debris mound. To complete the measurement of the water column, technical divers carried the EXO 1 sonde with them during sampling. Winch-operated water samples were also retrieved with a polyethylene FreeFlow bottle (HydroBios Kiel). The sampling depth of samples taken with the FreeFlow bottle represents the center of the sampling bottle and was determined by cable length with a depth counter attached to the winch. Furthermore, the EXO 1 probe was attached to the FreeFlow bottle to obtain the related *in situ* parameters and exact water depth of each water sample. Water samples taken by technical divers were collected by drawing up the water of the desired sampling depth into 140 ml sterile polyethylene Luer-Lock syringes with an attached three-way valve. The water depth and *in situ* parameters of samples taken by technical divers were determined with the EXO 1 sonde, which was attached to a side-mounted gas bottle and pointed toward the front. Water samples between 0 and 36 m were taken with the FreeFlow bottle, whereas samples taken between 36 and 52 m were collected by technical divers. All water samples were treated on-site immediately after retrieval. Water samples taken with the FreeFlow bottle were transferred into 140 ml sterile polyethylene Luer-Lock syringes with an attached three-way valve. From a total sampling volume of 140 ml, subsamples were taken for the determination of dissolved organic carbon (DOC) and dissolved inorganic carbon (DIC), cations, anions, on-site photometric analyses, and dissolved gases. Samples for the determination of dissolved ions and for subsequent photometric analysis of ammonium, nitrite, and sulfide were filtered through a cellulose acetate filter (0.22 μm) and transferred into 15 ml Falcon polypropylene centrifuge tubes. Samples for cation determination were acidified with 150 μl HNO_3 (32%) to adjust a pH <2.

2.3 | Water analysis

Cation concentrations of water samples were determined by optical emission spectroscopy with an Agilent 720 ICP-OES. Quality control was conducted using the reference materials SPS-SW1, SPS-SW2, and TMDA-70.2. Recovery rates were in the range of 94.5% and 102.4% for the analyzed elements. Concentrations of anions Cl^-, SO_4^{2-}, and NO_3^- were determined via ion chromatography (Dionex ICS-1100) with a recovery rate between 95% and 98% and a relative standard deviation (RSD) of <3% derived from long-term repeated analysis of reference material SPS-WW1 NUTR. The concentrations of DIC and DOC were determined with a Total Carbon Analyzer (Shimadzu TOC-CPH) with an RSD of <2% derived from repeated analysis of an in-house standard water. Sulfide, ammonium, and nitrite were determined on-site within 8 h after sample collection by photometric analysis using Merck Spectroquant® test kits (Sulfide Test for 0.020–1.50 mg L^{-1}, Ammonium Test for 0.010–3.00 mg L^{-1}, and Nitrite Test for 0.007–3.28 mg L^{-1}) and a Hach Lange DR200 Photometer. For quality control, charge balances of all water samples were calculated and the relative errors were below 5% in all analyzed samples, usually around 1% in freshwater samples and 1–5% in saline water samples. HS^- and HCO_3^- activities and calcite and gypsum saturation were calculated with PhreeqC (Parkhurst and Appelo, 1999) version 3.5.0 using phreeqc.dat. Diffusive ion fluxes (J) toward the redoxcline were calculated from linear regressions with the first Fick's law with diffusion coefficients (taken from phreeqc.dat; Parkhurst and Appelo, 1999) of DO_2, DNO_3^-, $DHCO_3^-$, and DHS^- of 2.1, 1.9, 1.2, and 1.8 * 10^{-9} m^{-2} s^{-1}, respectively.

2.4 | Determination of suspended particulate matter

The particulate matter content in water depths around the redoxcline was determined during the field trip from 13 to 25 of February 2020. Water samples with a high vertical resolution were obtained by a sampling device similar to that described by Jorgensen et al. (1979). This pump-based system allows for near-laminar inflow into the pump and thus minimizes vertical disturbances, which increases the vertical depth resolution to ~5 cm. The water was pumped at a rate of 0.3 L min^{-1} by a submersible Geo-Plus pump (COMET, Pfaffenschwende, Germany). The water flow was bypassed at the surface into a flow-through cell for continuous recording of *in situ* parameters with the multiparameter EXO 1 sonde (Xylem Analytics, Norway). Each depth level was pre-pumped for at least 10 min in order to get a minimum twofold exchange of the water volume in the system (pump, tube, and flow-through cell), and water samples were taken once the *in situ* values stabilized. The suspended particulate matter in the water was sampled by filtering a defined amount of water for each sample (20–60 ml) through syringe insert-type polycarbonate filters (0.22 μm). The loaded filters were subsequently flushed with 5–10 ml of distilled water in order to prevent the precipitation of salts from the remaining sample solution. Three filters were taken at each sampling depth, two for the quantification of bulk chemistry and one filter for the investigation with scanning electron microscopy (SEM). Immediately after sampling, the loaded filters were put in 50 ml centrifuge tubes (Sarstedt, Nümbrecht, Germany) for subsequent bulk quantitative element analyses. The SEM filters were placed into polystyrene containers and air-dried for about one day. Back in the laboratory, 2 ml of aqua regia (analytical grade HNO_3 and HCl) was added to the centrifuge tube with the loaded filters and heated for 60 min at 50 °C in order to dissolve the aqua regia dissolvable fraction of the particulate matter on the filters. The polycarbonate filter material is not dissolved as indicated by undetectable or very low metal and trace metal contents of blank filter and aqua regia controls. The minor contributions of the analyzed particulate element content might be attributed to the used aqua regia solution and leaching of polycarbonate filters (Supplementary data, https://doi.org/10.11588/data/GYLDH5). Subsequently, the tubes were filled with Milli-Q water up to a volume of 10 ml. This diluted supernatant solution was then subtracted and analyzed with Agilent 720 ICP-OES for Ba, Ca, Fe, Mg, Mn, P, S, Si, and Sr contents. The SEM filters were coated with carbon for scanning electron (SE) imaging and energy-dispersive X-ray (EDX) analyses. After SEM analysis, two carbon-coated filters were selected and additionally coated with gold for better resolved images of the particles. SE imaging and EDX analyses were performed with a Leo 440 at 20 kV with an X-Max 80 mm^2 detector.

2.5 | Microbiome sampling

To characterize the functional microbial diversity throughout the diverse sub-biotopes of the cenote, water samples were collected (during the sampling campaign from May 31 to June 6, 2018) from the respective water zones and depths: freshwater (32 m), central redoxcline (35.8 m), and halocline (38 m). Up to a water depth of 36 m, where the debris mount peaks, the water column was sampled using a winch-operated 1 L polyethylene FreeFlow bottle (HYDRO-BIOS, Kiel, Germany). Sampling of saltwater (below 36 m water depth) was conducted by technical divers. On site, 200 ml of the water samples were quickly filtered through a MCE membrane filter with a pore size of 0.22 µm (Merck KGaA, Darmstadt, Germany) to concentrate the microbiome. Subsequently, the filter was preserved in Allprotect Tissue Reagent/RNAprotect Bacteria Reagent (Qiagen, Hilden, Germany) at 4 °C to stabilize DNA/RNA until long time storage at −80 °C and further analysis. For 16S rRNA amplicon analysis, biological duplicates were taken; the metagenomic and metatranscriptomic data are based on one sample set that was sequenced with high depth due to limited possibilities to retrieve the samples with technical divers.

2.6 | DNA/RNA extraction

To extract the DNA, the filter membranes were washed once with 1x PBS to remove the Allprotect Tissue Reagent (Qiagen, Hilden, Germany). This solution was centrifuged for 5 min at 16,000 g to pellet and recover detached cells. The DNA pellet and the DNA attached to the filter membrane were purified using the DNeasy PowerWater Kit (Qiagen, Hilden, Germany) according to the manufacturer's protocol. IMGM Laboratories GmbH (Martinsried, Germany) conducted the isolation of RNA of water samples by means of the RNeasy PowerWater Kit (Qiagen, Hilden, Germany). Due to the very limited yield of RNA, no rRNA depletion was performed. For RNA, the total concentration and quality were measured with a Qubit 2.0 fluorometer (Life Technologies, Carlsbad, CA, USA) and a Bioanalyzer 2100 (Agilent Technologies, Santa Clara, CA, USA). For genomic DNA, a NanoDrop 2000 Spectrophotometer (Thermo Scientific, Waltham, MA, USA) and Qubit 2.0 was used. The samples were stored at −80 °C until further processing.

2.7 | Sequencing

16S rRNA gene amplicon, metagenome, and metatranscriptome sequencing was conducted by IMGM Laboratories GmbH (Martinsried, Germany). 16S rRNA amplicons were generated using the following primer sets: 341F (CCTACGGGNGGCWGCAG)/ 805R (GACTACHVGGGTATCTAATCC) for Bacteria and A519F (CAGCMGCCGCGGTAA)/ A906R (CCCGCCAATTCCTTTAAGTTTC) for Archaea (Stahl and Amann, 1991; Klindworth et al., 2013). Amplification and sequencing of bacterial and archaeal 16S rRNA genes was conducted on an Illumina MiSeq platform (Illumina, San Diego, USA) with paired-end 250 nt reads (PE250). For sequencing of metagenomic samples, the library preparation was conducted with the NEBNext Ultra II FS DNA library preparation kit (New England Biolabs, Frankfurt am Main, Deutschland). The libraries were sequenced on the Illumina NextSeq 500 platform (Illumina, San Diego, USA) with paired-end 150 nt reads (PE150) and a sequencing depth of at minimum 100 million reads. For metatranscriptome sequencing, the TruSeq total RNA Sample Prep Kit (Illumina, San Diego, USA) was used for library preparation and sequencing was performed on the Illumina NextSeq 500 platform with single-read 150 nt reads (SR150) and a sequencing depth of at minimum 100 million reads.

2.8 | Bioinformatic data analysis

After sequencing, the 16S rRNA gene amplicon data were processed using the Illumina software MiSeq Reporter (MSR) v2.5.1.3 and the Illumina Sequence Analysis Viewer (SAV) v1.9.1 for demultiplexing and trimming of adapter sequences. The analysis of the 16S rRNA amplicon datasets was conducted with the CLC Genomic Workbench Software 12.0 including the "Microbial genomic module 4.0" plugin. The amplicon data were quality-trimmed with a threshold of 0.05, followed by a primer trimming step and merging of paired reads. For taxonomic profiling, the OTU clustering was performed against the SILVA 16S database release v132 97%. For the duplicates of every sample, a mean value was calculated for every OTU. Very low abundant OTUs (minimum combined abundance less than 50) were removed. The first step in both metagenomic and metatranscriptomic analysis was the quality and adapter trimming of raw reads using the software tool Trimmomatic (v0.38) (Bolger et al., 2014) with the following parameters: "LEADING:3 TRAILING:3 SLIDINGWINDOW:4:15 MINLEN:105." Next, the metagenome high-quality paired-end reads were assembled using Megahit (v1.1.4–2) with the assembly settings of k-mer × 21–141 and steps of 20 (Li et al., 2015, 2016). As a next step, the prodigal software (v2.6.1) was used in -p meta mode to determine the coding sequences (CDS) within the assembled metagenome and to translate these into protein sequences (Hyatt et al., 2010). For the functional metagenome annotation, two approaches were used in combination. The protein sequences gained via prodigal were blasted against the Uniprot database (entry version 36, state: 28.05.2019) using DIAMOND (v0.9.24) blastp in sensitive metagenome mode allowing only one hit per query (Buchfink et al., 2015). Additionally, the eggNOG-mapper (v2.0.0) was used for orthology prediction and functional annotation via a protein-protein BLAST against the latest KEGG database (Huerta-Cepas et al., 2017, 2019). If the protein annotation differed between these two databases, the protein and nucleotide sequence of the respective gene was verified by another BLAST search against the NCBI database. For quantification of gene expression, the quality-trimmed metatranscriptomic reads were aligned against the metagenome CDS as reference index using Kallisto v0.45.0 (Bray et al., 2016) in default mode. For comparative analysis, the gene expression level was calculated in transcripts per million (TPM), which represents a normalization to gene length and sequencing depth.

To determine the diversity of the microbial community in the redoxcline water column based on the metagenomic and metatranscriptomic data, the quality-trimmed raw reads were mapped against the assembled metagenome using bowtie2 (v2.3.4.3) (Langmead and Salzberg, 2012) in default mode. The mapping result along with the quantitative information (abundance) was joined with the functionally annotated metagenome to include the taxonomic gene annotation achieved by the DIAMOND blast against the Uniprot database. Further, the number of reads was summarized on the taxonomic level of order and family. For these two steps, a custom python-based script was written (provided Data S1 in Supporting Information, file name "lappleb.py"). To verify the result, another 16S rRNA-based approach was followed by using phyloFlash (v3.3beta1) that reconstructs and analyzes the SSU rRNAs genes to improve the determination of the phylogenetic composition (Gruber-Vodicka et al., 2020).

To amend the functional analysis with further taxonomic information, a binning of the contigs was conducted using MetaBAT2 with default configuration after bowtie2 mapping of filtered reads to the assembly (Kang et al., 2019). The quality of recovered genomes was validated using CheckM (Table S1) (Parks et al., 2015). The binning information was added to the metagenome annotation (based on unbinned contigs; Tables S2–S5). The metatranscriptomic reads were also mapped against the bins using Kallisto to verify the transcriptional activity of taxonomic units (Figure S2).

3 | RESULTS

3.1 | Hydrogeochemistry

Previous studies proposed the redoxcline, which overlaps with the turbid layer, as the water layer in which calcite is precipitated (Ritter, 2020; Ritter et al., 2019). Here, we conducted a specific study that targeted the hydrogeochemical profile of the turbid layer at the time of microbiome sampling. The stratified water column of the cenote comprises a freshwater body (0–36.6 m), a halocline (36.6–46 m), and a saltwater body (below ~46 m) (Figure 1c). Water temperatures within the freshwater body and redoxcline are around 25 °C showing only little variation throughout the year (Ritter, 2020). At the top of the halocline, a 1.6-m-thick white, cloudy turbid layer in the water depth of ~35.0–36.6 m is indicated by the peak of turbidity of up to 7 FNU (formazin nephelometric units) in the center of the turbid layer (Figure 2). The turbid layer overlaps with the redoxcline, in which the redox potential (EH) changes significantly from +400 to −150 mV.

The pH values were circumneutral in the freshwater and decreased marginally to 6.84 immediately above the increase in turbidity at the water depth of 35.3 m. Within the redoxcline, the pH values showed a distinct peak of 6.91 at the center of the layer. Below, pH values continuously decreased to minimum values of 6.56 at 42 m water depth. The concentration of dissolved oxygen (DO) decreased downwards toward the turbid layer and was below the detection limit at the top of the turbid layer (Figure 2). Similarly, the concentrations of nitrate (~30 μmol L^{-1} at 34 m) and nitrite (~1.5 μmol L^{-1} at 34 m) decreased from above the turbid layer toward its center. In contrast, the concentrations of ammonium (~0.22 mmol L^{-1} at 38 m), sulfide (~1.1 mmol L^{-1} at 38 m), and bicarbonate (~7.25 mmol L^{-1} at 38 m) decreased from below the turbid layer toward its center. Importantly, the saturation indices (SI) indicated calcite saturation in the freshwater body with SI values of 0.02–0.04 above the turbid layer and calcite undersaturation in the halocline with SI values of down to −0.32 at ~40 m water depth. A distinct peak toward oversaturation was identified in the center of the turbid layer with SI values of up to ~0.11 at 36 m (Figure 2).

3.2 | Particulate matter in the redoxcline

In connection with the central question of whether the turbid layer is formed by microbially induced inorganic calcite precipitation and whether the process of nitrate-driven sulfide oxidation plays a role in this process, particulate calcium and sulfur were quantified in the redoxcline. The respective solid phases were analyzed by scanning electron microscopy (SEM) and energy-dispersive X-ray spectroscopy (EDX). As the pH is a central controlling factor of calcite precipitation in the redoxcline, the question arises whether zero-valent sulfur (as an intermediate product or end product of an incomplete oxidation) is indeed present in higher concentrations in the electron

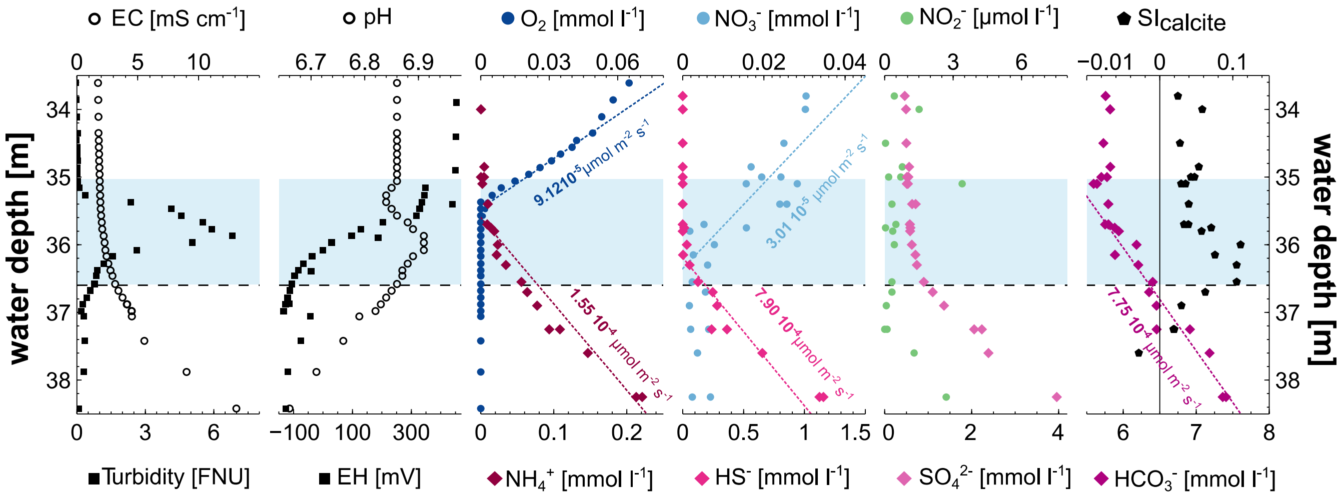

FIGURE 2 Hydrogeochemistry of cenote El Zapote showing the pelagic redoxcline (gray), the oxic fresh water above and the anoxic halocline below. Besides the electric conductivity (EC) in mS cm^{-1}, the turbidity in FNU (formazin nephelometric units), the pH and the redox potential (EH) in mV, the concentrations of O_2, NH_4^+, NO_3^-, HS^-, NO_2^-, SO_4^-, and HCO_3^- were determined (data from 2018). $SI_{calcite}$ was calculated with PhreeqC using phreeqc.dat. The fluxes J are given in μmol m^{-2} s^{-1}

acceptor-limited turbid layer or rather sulfate (as product of the complete oxidation). The reactions leading to these two products would have opposite effects on the pH. Whereas the incomplete oxidation of sulfide to elemental sulfur would result in an increased local pH (Kamp et al., 2006) and, thus, promote calcite precipitation, the production of sulfate may induce acidification and calcite dissolution. The *in situ* parameters (Figure 2) suggest that no sulfate accumulated in the turbid layer. The particulate matter in the redoxcline was sampled in another sampling campaign using an optimized sampling system (see Materials and Methods section 2.4) that allows minimal vertical disturbances during sampling and thus an increased vertical water profile resolution of ~5 cm. Similar to Figure 2, Figure 3 shows the same pattern for the electrical conductivity and redox potential as described. However, the center of the redoxcline was about 0.8 m higher (~34.9 m) than in 2018 (~35.7 m; Figure 2). With the implementation of the optimized water sampling system, the pH profile could be resolved much higher, ranging from about 6.88–7.04 and falling back to ~6.9 with increasing water depth toward the halocline. Regarding turbidity, the values were twice as high as measured before in 2018 at the most pronounced point (Figure 2). Ca and S were by far the most abundant elements found on the filters (100–1,100 μg L^{-1}), while Mg, Sr, and Ba as minor constituents of carbonate minerals were also found on every filter (1–200 μg L^{-1}). Fe and Mn showed only trace contents (0.002–8 μg L^{-1}), which could also be due to incorporation into carbonate minerals or contamination as indicated by the high blank values for Mn (Table S6). Si contents around 20 μg L^{-1} indicate that some silicate phases were also present on the filters, which might be detrital. Both particulate calcium and sulfur were clearly detectable in the redoxcline water filtrates (Figure 3). While in the adjacent freshwater only $<$ 2 μmol L^{-1} (~33 m depth) particulate calcium was measured, a strong increase from the top of the turbid layer to the maximum value of ~28 μmol L^{-1} was detected in the center of the turbid layer. The concentration decreased from there on toward the lower end of the turbid layer. The same trend could be measured for particulate sulfur with a maximum value of ~29 μmol L^{-1}. Both concentration curves coincide very well with the measured turbidity; also the peaks overlap at a water depth of ~34.9 m. The highest pH value, however, was detected slightly below the maxima in turbidity, particulate calcium, and sulfur. Just as predicted from the SI values for calcite (Figure 2), these data point toward the redoxcline as the location for calcite precipitation with the focus point in the center of the turbid layer.

SEM and EDX analysis of parallel filters showed that the particulate Ca is derived from numerous 4–10-μm-sized Ca-carbonate particles (Figure 4b). Additionally, minor amounts of silicate particles such as diatom remains, and sand or dust grains, were present (Figure 4h). The Ca-carbonate particles were interpreted as well-crystallized calcite minerals showing various rhombic (Figure 4b,f) and aggregations of small sparry minerals (Figure 4a, e and g) that often appear to have grown or formed around crystallization seeds (Figure 4e and h). Pure S-phases or other solid phases containing enough sulfur to explain the analyzed bulk S contents could not be clearly identified by EDX analyses. Although every calcite phase contained several percent sulfur (Table S7), incorporation of sulfur into calcite does not explain the apparent lack of sulfur phases on the SEM-analyzed filters. Accumulations of smaller ~0.1–0.3-μm-sized globules were frequently observed on the filters (Figure 4a–d and g). When analyzed by EDX, these spots with globule accumulations generally show elevated amounts of sulfur compared with areas on the filters with no particles (Table S7). The vacuum conditions of the SEM chamber can

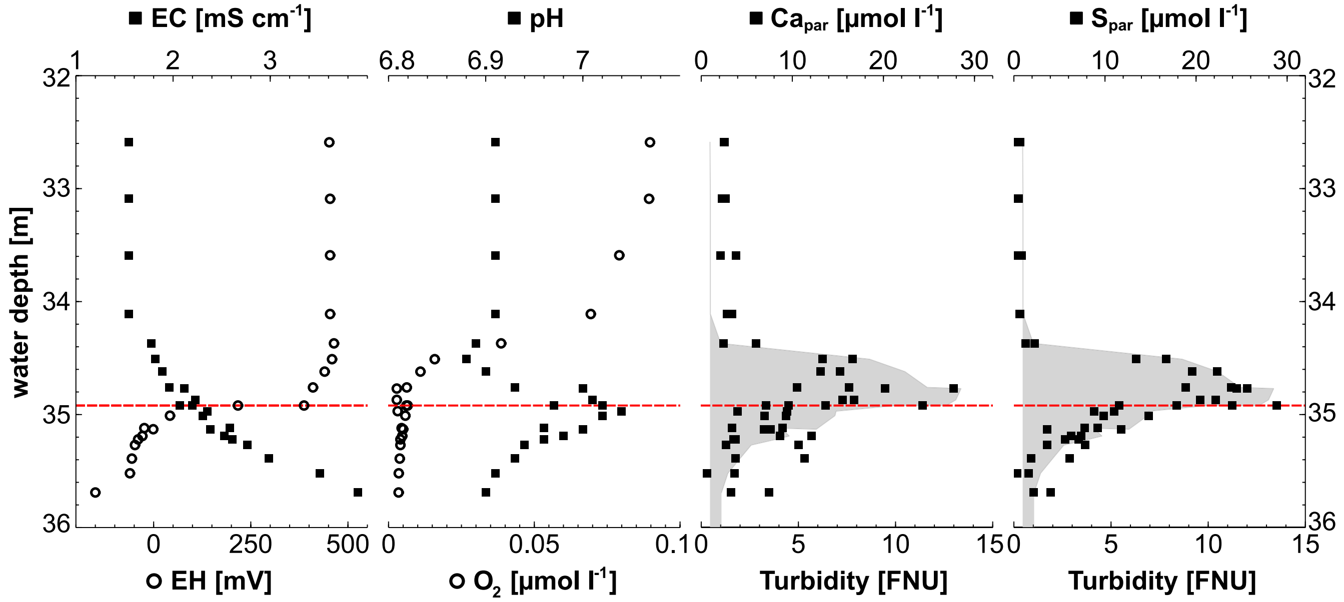

FIGURE 3 Quantification of particulate sulfur and calcite in the redoxcline of El Zapote. The presence of particulate sulfur and calcium (in μmol L^{-1}) was analyzed in the redoxcline in the context of the following environmental parameters (data from 2020): the redox potential (EH) in mV, the electric conductivity (EC) in mS cm^{-1}, the pH, the turbidity in FNU (formazin nephelometric units), and the oxygen concentration in μmol L^{-1}. The red dashed lines indicate the water depth below which free sulfide was detected. The gray marking represents the turbid layer

cause sublimation of S(0), and the electron beam can rapidly transform or burn sulfur material (Nims et al., 2019). Since the electron beam covers an area of at least ~2 μm in diameter, the elevated sulfur content in areas with globule accumulations is so far the best analytical evidence for the identification of the sulfur-bearing solid phases. The two gold-coated filters revealed that the globule accumulations were enclosed into 2–4-μm-sized oblate structures (Figure 4a, c and g). The globules were brighter than the large calcite grains nearby, indicating that the globules consist of an element heavier than Ca and C, like S.

3.3 | Microbial diversity

We hypothesized that the pelagic turbid layer is a specific reaction compartment, which is stabilized in its sharp gradients by the activity of microorganisms. Moreover, microbial activity could set the foundation for calcite precipitation and the formation of the turbid layer. Hence, a 16S rRNA-based community analysis was conducted, to determine whether the turbid layer is a zone that is simply characterized by a gradual transition of one community composition into the other or alternatively, whether it contains unique groups that

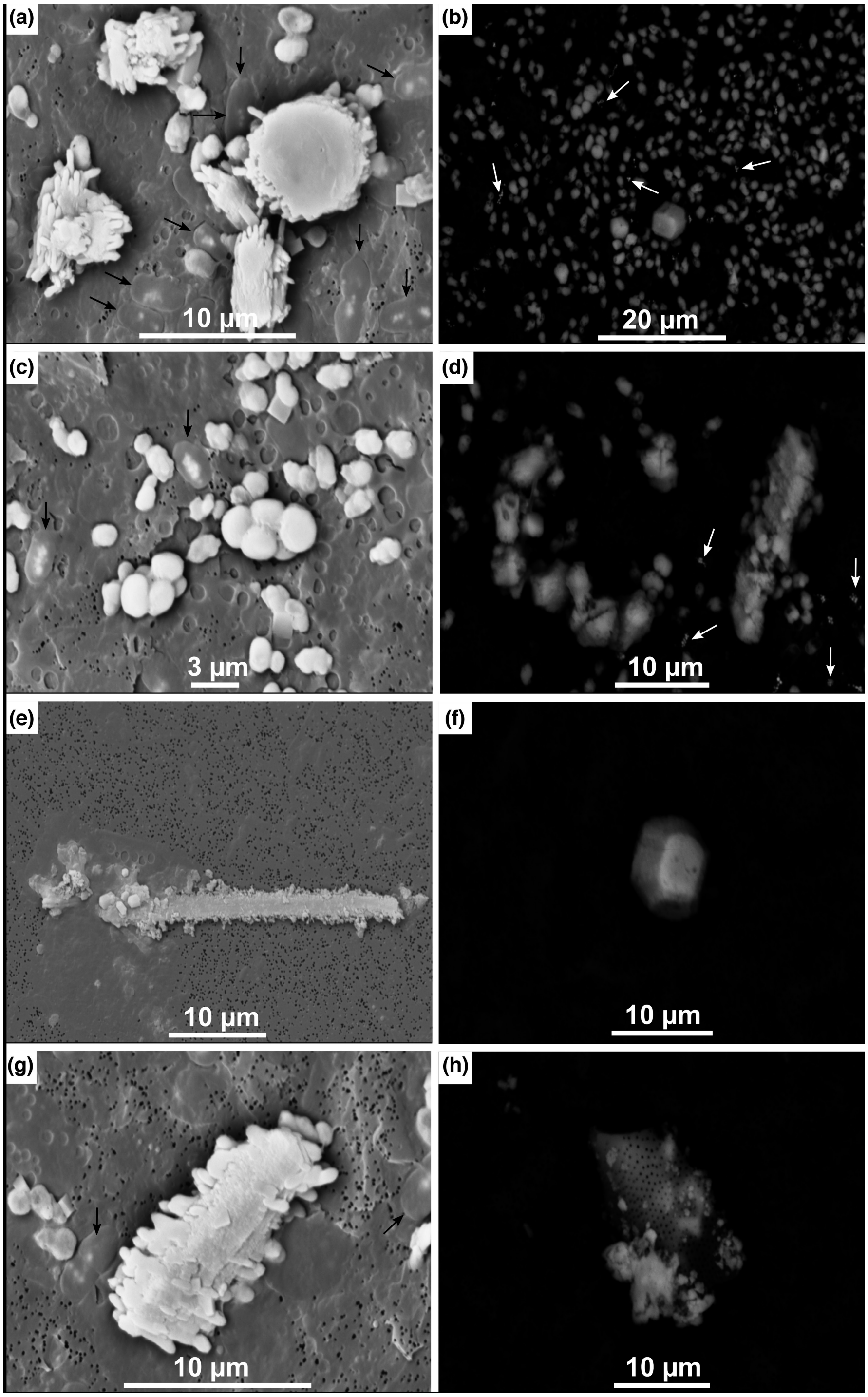

FIGURE 4 SEM images of gold-coated (left) and carbon-coated (right) filter samples of the redoxcline of cenote El Zapote. (a) 2–9-μm-sized calcitic particles; black arrows point toward bright 0.1–0.3-μm-sized globules, which agglomerate in 2–4-μm-sized oblate structures most likely representing intracellular elemental sulfur. (b) 3–5-μm-sized calcite crystals surrounded by many 1–2-μm-sized smaller calcite crystals; white arrows point toward globule agglomerations similar to (a). (c) 1–4-μm large partially coherent calcitic particles of different shapes; black arrows point toward globule agglomerations within oblate structures similar to (a). (d) Differently sized calcite particles and globule agglomerations (marked by white arrows). (e) Approx. 30-μm-long calcitic particle with finely structured grain boundaries. (f) 8-μm-sized rhombic calcite crystal with idio- to hypidiomorphic surfaces. (g) Approx. 7-μm-long calcitic particle with mostly rounded 1–2-μm calcitic grain edges and globule agglomerations similar to (a) (black arrows). (h) Approx. 16-μm-sized siliceous shell structure with calcitic particle growing on its lower edge

strongly increase in concentration compared with the adjacent water layers. Based on the 16S rRNA gene amplicons (Tables S8 and S9), the relative abundance of different microbial phyla (Tables S10 and S11) was determined in the freshwater layer (sampled at 32 m), the redoxcline/turbid layer (sampled at 35.8 m), and the halocline (sampled at 38 m). The microbiome detected in the redoxcline differed markedly from the surrounding water layers by the dominance of Proteobacteria (63%), which were significantly less abundant in the adjacent freshwater layer (30%) and the halocline (17%) (Figure 5). The abundance of the phylum Actinobacteria was particularly high in the freshwater with 49% and decreased from the redoxcline with 11% to 3% in the halocline. In contrast, Chloroflexi (17%) and especially Epsilonbacteraeota (32%) were dominant in the halocline, but their abundance decreased toward the turbid layer, while they were absent in the freshwater. Bacteroidetes were almost equally present in both redoxcline (5%) and halocline (4%) and were absent in the freshwater. The archaeal diversity was highest in the halocline. Bathyarchaeota (27%), Euryarchaeota (26%), and Thaumarchaeota (47%) were detected, whereas the freshwater exclusively contained Thaumarchaeota (100%). In the redoxcline, Thaumarchaeota dominated the archaeal composition with 99% relative abundance, while Bathyarchaeota comprised only 1%. The overlapping redoxcline and turbid layer thus represent a microbial transition zone between the freshwater and the halocline that is dominated by Proteobacteria.

In agreement with the 16S amplicon sequencing data, the dominant taxon identified by metagenomic and metatranscriptomic analyses was the order Hydrogenophilales belonging to the Proteobacteria. Some of the reads were further assigned to the Hydrogenophilaceae (Figure 6). Surprisingly, the family Nitrosopumilaceae (belonging to the Thaumarchaeota) was underrepresented in the metagenome (<2%) but appeared to be the second most abundant in the metatranscriptome (13%) following the Hydrogenophilales/Hydrogenophilaceae (together 35%). The abundance of other families varied only marginally when both data sets were compared. According to the 16S rRNA gene sequence from the amplicon data set, the Hydrogenophilales were not further classifiable than to the level of "uncultured Hydrogenophilaceae." The sequence alignment to the SILVA database (v132) revealed an identity of 93.7% to "uncultured Hydrogenophilales" and 92.8% *Annwoodia aquaesulis* (of the order Nitrosomonadales) according to the NCBI 16S ribosomal RNA database. The abundance and high activity of members related to the Hydrogenophilales were further verified by a metagenomic binning. Bin 86 comprised the highest translational activity (35.4%) and contained the key genes for the major metabolic processes described in the section below.

3.4 | Metatranscriptome-based metabolic profiling

Metatranscriptomic and metagenomic analysis was used to address the question whether microbial activity could be a central catalyst for subaqueous calcite precipitation by increasing the local pH in the turbid layer. The metagenome assembly of the redoxcline revealed 1,068,412 contigs with a total of 849,570,422 bp. A summary of the quantitative sequencing results (metatranscriptome and metagenome) is given in the Supporting Information, Table S12. The average

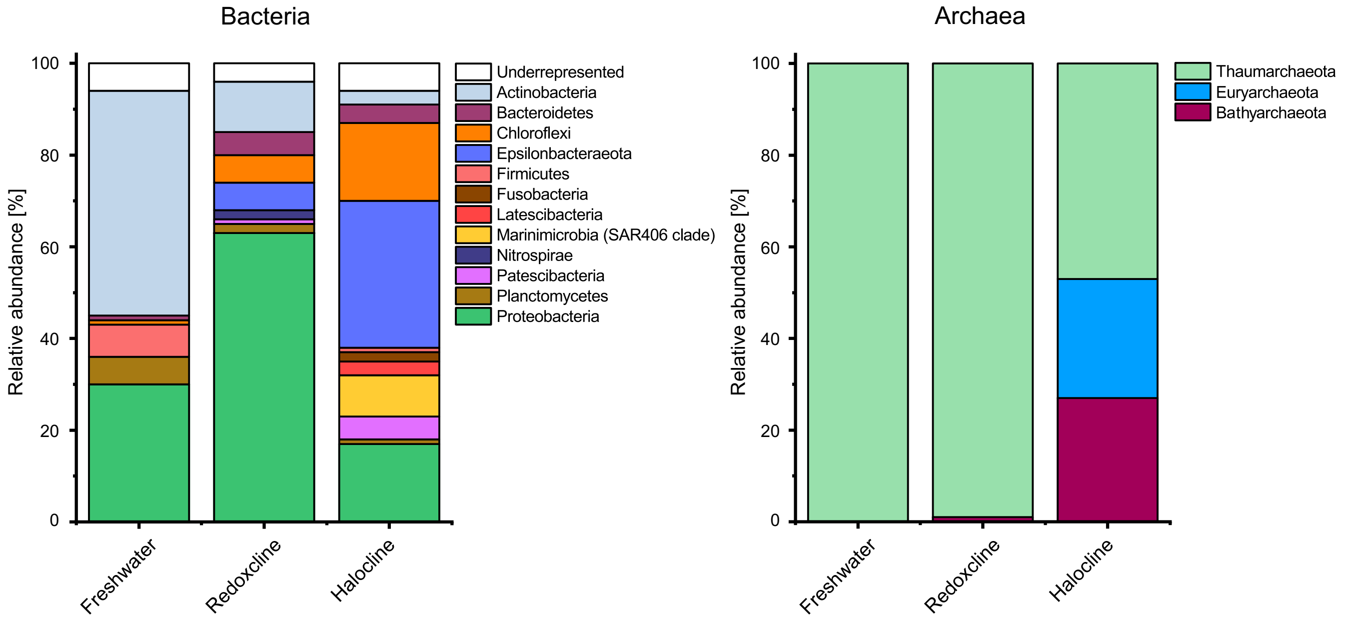

FIGURE 5 Relative abundance of OTUs of Bacteria (left) and Archaea (right) throughout the water column of the cenote. The microbial diversity (based on 16S rRNA gene amplicon sequencing) in the planktonic phase was analyzed in the different water layers (freshwater, redoxcline, and halocline). Depending on the respective sample, 100% = 71–102,000 reads for Bacteria and 24–117,000 reads for Archaea in OTUs (Table S8–S11)

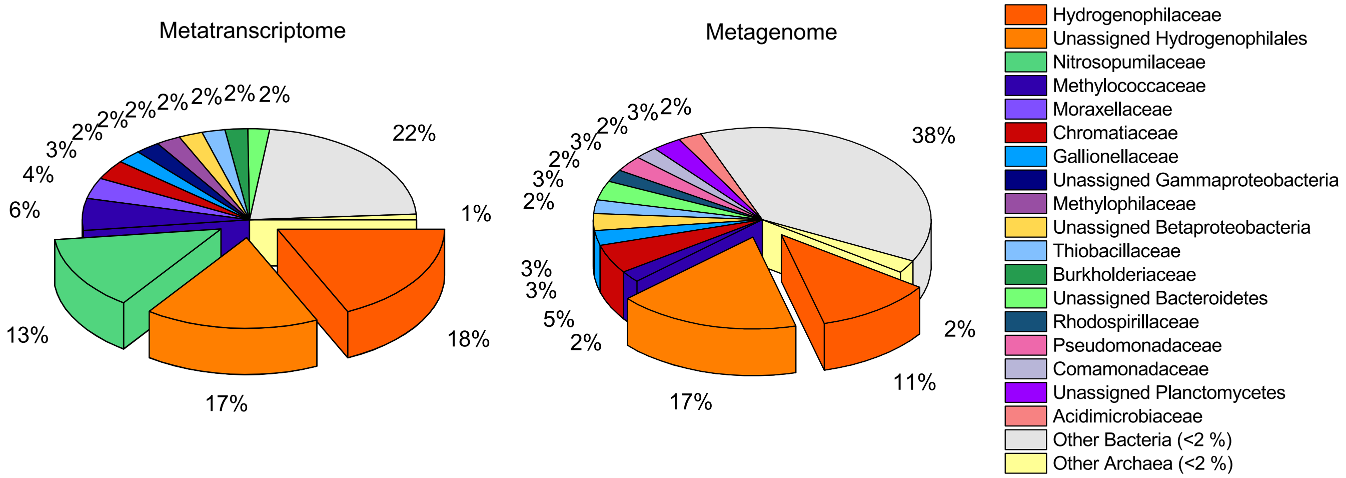

FIGURE 6 Microbial diversity in the water column of the pelagic redoxcline of cenote El Zapote. Relative abundance based on the taxonomic annotation of metatranscriptomic (left) and metagenomic raw reads (right)

contig size is 795 bp (minimum 200 bp and maximum 312,582 bp). The N50 value was 996 bp. Binning of metagenomic contigs generated 132 bins. Only 3% of all contigs were binned, which represent 24% of the assembled nucleotides. Only 27.8% of the metatranscriptome could be mapped to the binned metagenome but 60% to the unbinned metagenome. The metatranscriptome analysis based on the binned metagenome revealed many deficits in the elucidation of the central metabolic pathways. Therefore, the data presented are based on the unbinned approach, which provided significantly more holistic information, as a much larger proportion of the metatranscriptome was mapped and integrated. For further taxonomic assignment of these contigs, the binning information was subsequently added. Nevertheless, important information like several key genes in the nitrogen cycle was discarded in the binning process. Therefore, this analysis focuses on the annotation of all (including unbinned) contigs.

Figure 7 (based on Tables S2–S5) compares the expression levels (in transcripts per million (TPM)) of genes involved in the nitrogen and sulfur cycles, photosynthesis, and autotrophy. In case of the nitrogen and sulfur cycles, which seemed to dominate in the turbid layer, the abundances of the respective gene transcripts are additionally shown in the context of their metabolic pathways (Figure 8, scheme based on Alvarez et al. (2014) and Rodionov et al. (2005); Figure 9, scheme based on Grabarczyk and Berks (2017)).

Within the nitrogen cycle, the gene transcripts of the ammonium monooxygenase (subunit A, *amoA*) reached the highest abundance (548 TPM) among all marker genes of the nitrogen cycle (Figures 7 and 8). Transcripts for the hydroxylamine oxidoreductase (*hao*), the second enzyme relevant for the complete oxidation of ammonium to nitrite, were only low abundant with 4 TPM. A similarly low abundance (14 TPM) was measured for the nitrite oxidoreductase (*nrxA*) that catalyzes the oxidation of nitrite to nitrate, the last step in nitrification. The microbial community also expressed all marker genes involved in the process of denitrification, such as the nitrate reductases *narG* (48 TPM) and *napA* (246 TPM), the nitrite reductases *nirK/S* (335 TPM), the nitric oxide reductase *norB* (195 TPM), and nitrous oxide reductase *nosZ* (507 TPM). In fact, *nosZ* was the most abundant gene transcript of the denitrification pathway. On the contrary, dissimilatory nitrate reduction to ammonium (DNRA) and anaerobic ammonium oxidation (anammox) seemed to play a minor role. Transcripts encoding the catalytic subunits of two different nitrite reductases, *nrfA* and *nirB*, involved in the DNRA were only weakly abundant (8 and 11 TPM). Hardly any transcripts were found for anammox-specific genes such as the hydrazine synthase (*hzs*) and the hydrazine dehydrogenase (*hdh*). Apparently, denitrification and oxidation of ammonium are the main reaction cascades of the nitrogen cycle in the turbid layer.

Two genes of the sulfur cycle exceeded all other genes in their transcript abundance by far (Figures 7 and 9). They encode the central component of the periplasmic sulfur oxidation (Sox) system, the heterodimeric SoxYZ carrier protein. A total of 2,919 and 3,684 TPM could be assigned to *soxZ* and *soxY*, respectively. In this complex, SoxY covalently binds reduced sulfur species at its C-terminal cysteine persulfide residue (Figure 9) (Sauvé et al., 2007). The complete Sox system also comprises the proteins SoxB (146 TPM; Figures 7 and 9), SoxXA (372 TPM for *soxX*, and 767 TPM for *soxA*), and SoxCD (*soxC*, 2 TPM; *soxD* 0 TPM) (Rother et al., 2001). SoxXA catalyzes the initial step of the Sox cycle, in which sulfide, thiosulfate, elemental sulfur, and other inorganic sulfur compounds are added to the SoxY-cysteine persulfide. In the next step, SoxB hydrolyzes the terminal sulfonate group and releases sulfate. SoxCD in turn oxidizes the terminal sulfane sulfur at SoxY to another sulfonate group, which is also hydrolyzed by SoxB with the release of sulfate and the SoxYZ persulfide (Grabarczyk & Berks, 2017; Rother et al., 2001). Compared with *soxXA*, the respective transcription level for *soxB* was distinctly lower. In line with this result, we could not detect increasing sulfate concentrations in the redoxcline (Figure 2). Transcripts of genes encoding the SoxCD protein were almost not detectable. Instead, organisms that lack the *soxCD* genes transfer the sulfane sulfur to sulfur globules to regenerate the carrier protein SoxYZ (Frigaard &

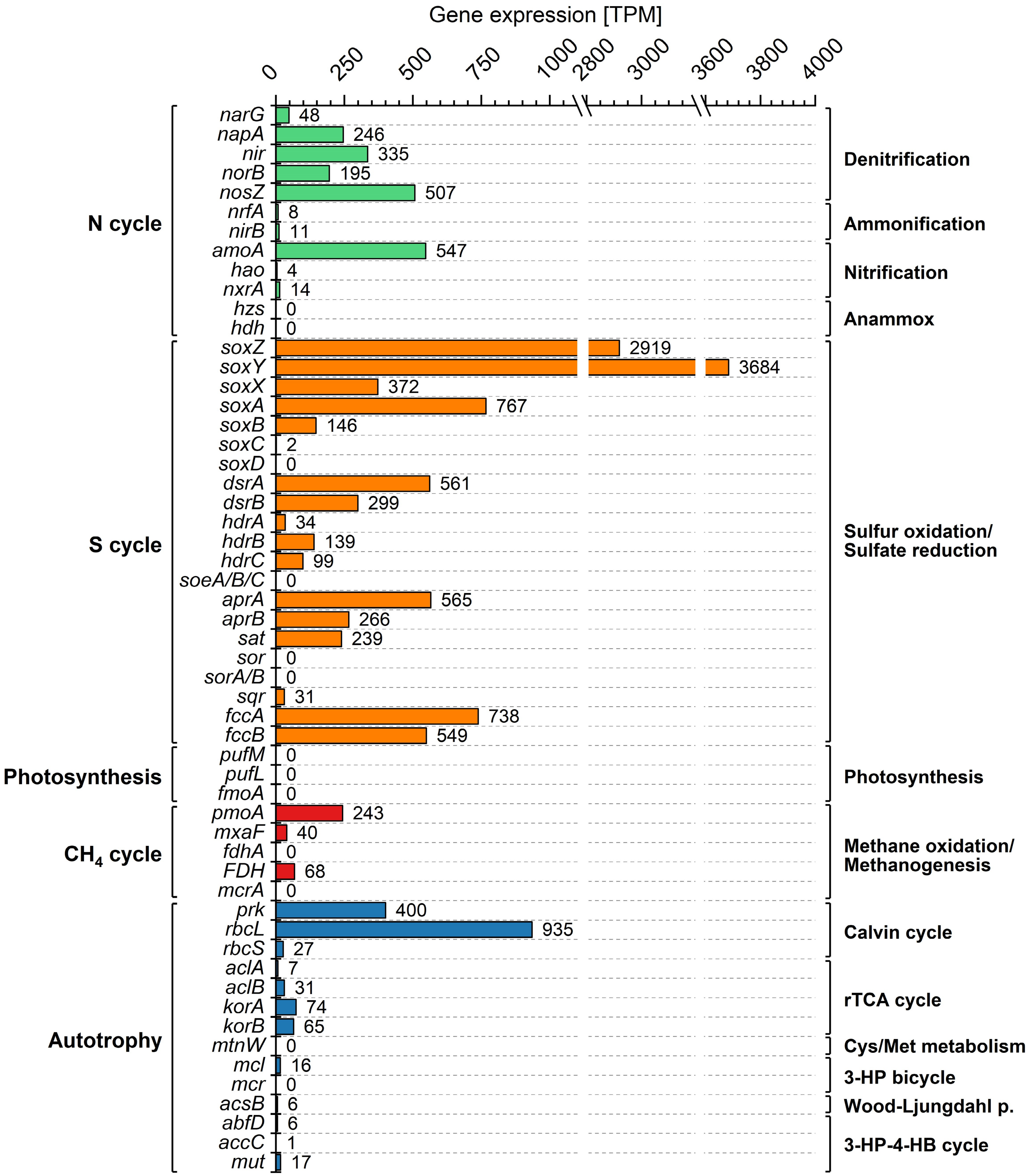

FIGURE 7 Metatranscriptomic profiling of the planktonic microbiome in the redoxcline of cenote El Zapote. Abundance of gene transcripts (in transcripts per million [TPM]) involved in the N cycle (green), S cycle (orange), photosynthesis (violet), and autotrophy (blue)

Dahl, 2008; Sauvé et al., 2007). Of note, sulfur particles have been previously detected in the redoxcline and turbid layer of El Zapote (Ritter et al., 2019).

Sulfide/H_2S cannot be oxidized only by the Sox complex but also by two other proteins producing polysulfide and/or S^0. The periplasmic flavocytochrome *c* FccAB transfers electrons at the cytochrome *c* level into electron transport chains (Oh-oka & Blankenship, 2004), whereas the membrane-bound sulfide:quinone oxidoreductase (SQR) catalyzes the same reaction, only coupling sulfide oxidation to the quinone pool (Chen et al., 1994; Griesbeck

FIGURE 8 Gene expression levels of genes involved in pathways of the nitrogen cycle. Metatranscriptomic profiling of the microbiome in the planktonic phase of the pelagic redoxcline of El Zapote. Abundance of gene transcripts (in transcripts per million [TPM]) of the catalytic subunits of the respective enzyme is shown in dark blue. Scheme based on Alvarez et al. (2014) and Rodionov et al. (2005)

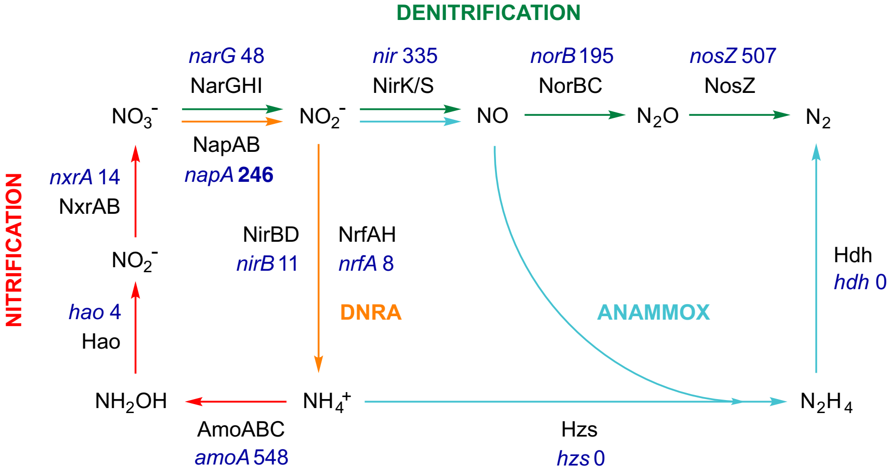

FIGURE 9 Abundance levels of gene transcripts involved in pathways of the sulfur cycle. Metatranscriptomic profiling of the microbial community in the planktonic phase of the pelagic redoxcline of El Zapote. Abundance of gene transcripts (in transcripts per million [TPM]) is shown in dark blue. Reactions with dashed arrows occur in the cytoplasm, the ones with solid arrows in the periplasm. Sox cycle according to the revised version by Grabarczyk and Berks (2017)

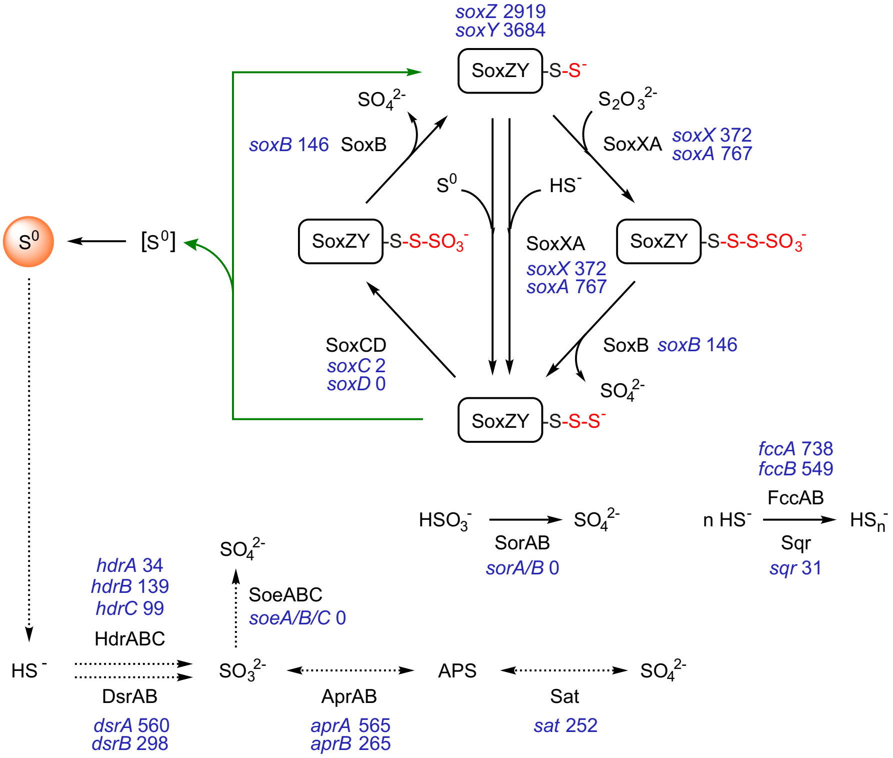

et al., 2002; Marcia et al., 2009; Oh-oka & Blankenship, 2004; Reinartz et al., 1998). The high abundance of *fccA/B* transcripts (*fccA/B* 738/549 TPM) indicates that this is potentially a further mechanism that sustains the observed sharp sulfide gradient. Transcripts for *sqr* were much lower in abundance (31 TPM; Figure 9). Thus, FccAB and the Sox complex seem to represent the major sulfide sinks in the turbid layer community, with less contribution from SQR.

Although we could not detect increasing sulfate concentrations in the redoxcline and revealed the presence of particulate sulfur, it became also evident that cytoplasmic processes will at least to some extent lead to a further oxidation of sulfur species toward sulfate. Core of this oxidative reaction cascade are the enzymes DsrAB, APS, and Sat. The dissimilatory sulfite reductase (rDsrAB) transfers electrons to acceptors such as NAD^+ producing sulfite (Löffler et al., 2020). Sulfite is subsequently converted by the adenylyl-sulfate reductase (AprAB) to adenosine-phosphosulfate (APS) (Frigaard & Dahl, 2008; Stockdreher et al., 2014; Tanabe et al., 2019). The final enzyme sulfate adenylyltransferase (Sat) completes the formation of sulfate coupled to ATP synthesis by substrate-level phosphorylation (Frigaard & Dahl, 2008). These three enzymes are involved in both sulfide oxidation and sulfate reduction (Figure 9). To clarify which direction of these two metabolic processes prevails, *dsrAB* sequences of the main key players (see below; Figure 10) were compared against the *dsrAB*-database established by Müller et al. (2015) using the blast algorithm. Via this classification system, we determined that the dominant *dsr*-expressing orders Hydrogenophilales, Thiotrichales, and Nitrosomonadales (Figure 10) most probably express the reverse, oxidizing form of DsrAB (Tables S13–S15). Hence, microbes in the planktonic phase of the redoxcline/turbid layer are likely not

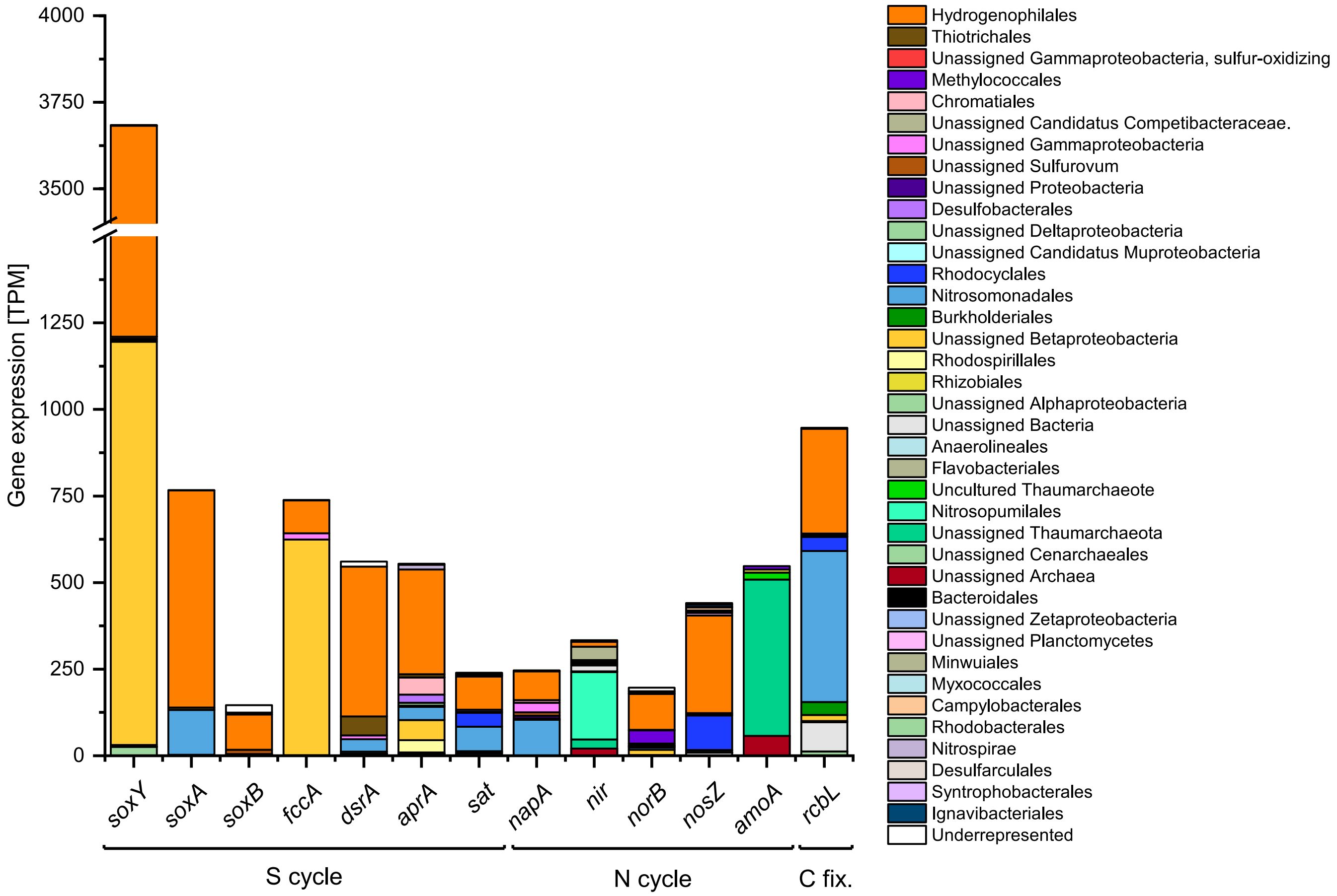

FIGURE 10 Taxonomic assignment of transcripts of identified key genes. Metatranscriptomic profiling of the microbiome in the planktonic phase of the pelagic redoxcline of El Zapote. To identify the microbial key players, the determined most relevant genes for the metabolism in the redoxcline were analyzed taxonomically. Abundances in transcripts per million [TPM]

conducting dissimilatory sulfate reduction. The genes for the heterodisulfide reductase Hdr, which is also proposed to be involved in sulfite production (Boughanemi et al., 2016; Koch & Dahl, 2018), were moderately expressed (*hdrA*/*B*/*C* 34/139/99 TPM). Overall, cytoplasmic processes leading to sulfate production seem to be active but—considering the *fccAB* and *sox* gene expression—probably on a lower level compared with periplasmic sulfide oxidation. It is important to note that all of these sulfur compound oxidation processes work in the absence of O_2 (most also in its presence) and can thus be coupled to nitrate/nitrite reduction. Accordingly, transcripts for oxygen-dependent enzymes such as sulfur oxygenase reductase were not found (*sor* 0 TPM; not to be confused with *sorAB*).

We also addressed the question if the process of photosynthesis still plays a role in the center of the turbid layer in the water depth of 35.8 m. The genes of apocytochrome *f* of the cytochrome b_6f complex (*petA*), the photosystem II P680 reaction center D1 protein (*psbA*) (Mulo et al., 2009), photosystem I P700 chlorophyll *a* apoprotein A1 (*psaA*)(Fromme, 1996), and the geranylgeranyl diphosphate/geranylgeranyl bacteriochlorophyllide reductase (*bchP*), which is relevant for the synthesis of bacteriochlorophyll (Addlesee & Hunter, 1999; Shi et al., 2005), were apparently not or only marginally expressed (<1 TPM). Likewise, the expression of four marker genes for anoxygenic photosynthesis was—if at all—negligible (Imhoff, 2016) (Figure 7). Thus, light as energy source seems to be limited and photosynthesis is not a major process in the turbid layer.

Autotrophic microbes can increase the pH in their microenvironment, which is relevant for calcite precipitation. This seems to be particularly due to the uptake of HCO_3^- and the consequent intracellular conversion to CO_2 by carbonic anhydrases (Görgen et al., 2020). Bacteria and Archaea can fix carbon dioxide via various pathways, and the individual occurrence correlates with certain niche characteristics (Figure 7). Transcripts of genes encoding the phosphoribulokinase (*prk* 400 TPM) and especially the ribulose-bisphosphate carboxylase (rubisCO; *rbcL* 935 TPM, *rbcS* 27 TPM) of the Calvin cycle exceeded the abundance of all marker gene transcripts of other autotrophic pathways by far (reverse TCA cycle, 3-hydroxypropionate (3-HP) bicycle, Wood-Ljungdahl pathway, and 3-hydroxypropionate/4-hydroxybutyrate (3-HP/4-HB) cycle). Next to the *soxYZ* gene transcripts, the *rbcL* mRNA was the second most abundant. However, a group of microorganisms also seemed to fix carbon dioxide via the reverse TCA cycle as the key transcripts encoding the 2-oxoglutarate ferredoxin oxidoreductase (*korA* 74 TPM, *korB* 65 TPM) and ATP citrate lyase (*aclA* 7 TPM; aclB 31 TPM) were also detectable. Although transcripts that could be assigned to members of the Thaumarchaeota were highly abundant in the metatranscriptome, we could detect only low transcript levels of key genes for the 3-HP/4-HB cycle.

3.5 | Microbial key players

Determination of the potential microbial key players in the redoxcline involved in the formation of the turbid layer was based on a taxonomic assignment of transcripts encoding key enzymes (Figure 10; based on Tables S16). The main focus was on the genes of the dominant pathways such as sulfur oxidation, denitrification, oxidation of ammonium, and carbon dioxide fixation via the Calvin cycle.

Notably, *soxY* transcripts of the SoxYZ sulfur carrier protein for sulfur oxidation were dominantly expressed by the order Hydrogenophilales with 2472 TPM, followed by unassigned β-Proteobacteria with 1164 TPM. Also, *soxA* and *soxB* were dominantly expressed by Hydrogenophilales. Periplasmic FccA was mainly expressed by unassigned β-Proteobacteria and the order Hydrogenophilales. Moreover, most *dsrA* reads could also be assigned to the Hydrogenophilales, followed by the orders Thiotrichales and Nitrosomonadales and were classified as belonging to the oxidative type of DsrAB (Tables S13–S15). Both Nitrosomonadales and Hydrogenophilales also expressed *aprA* and *sat*. The nitrate reductase catalytic subunit gene *napA* was almost equally expressed by Hydrogenophilales and Nitrosomonadales. Besides *napA*, the order Hydrogenophilales also expressed all other denitrification marker genes, such as *nir*, *norB*, and *nosZ*. Surprisingly, not only the *amoA* gene for ammonium monooxygenase subunit A was mostly expressed by Thaumarchaeota, and more specifically by the family Nitrosopumilaceae, but also the *nir* genes encoding the nitrite reductase. The highest proportions of large subunit transcripts of the RubisCO (*rbcL*) were assigned to the orders Hydrogenophilales and Nitrosomonadales and to a minor part to Rhodocyclales and Burkholderiales.

Concerning the key genes of the denitrification and sulfur oxidation pathway within the binned metagenome, the highest expression values were assigned to bin 86, which in turn most likely comprises a population of the order Hydrogenophilales (Tables S2–S5). The Hydrogenophilales dominate the sulfur cycle as indicated by the high *soxY* and *dsrA* expression levels. They also expressed all genes relevant for the complete reduction in nitrate to dinitrogen and seem to fix carbon dioxide via the Calvin cycle. The same applies to the Nitrosomonadales; however, it is unclear whether the high levels of *soxY* transcripts from unassigned β-Proteobacteria can also be assigned to them. In the nitrogen cycle, the Thaumarchaeota seem to be key players as they predominantly express *amoA* and *nir* genes.

4 | DISCUSSION

The formation of a pelagic redoxcline requires a seasonal or permanent stratification of the water body. Consequently, pelagic redoxclines typically occur in water bodies partially isolated from the open ocean, for example, marine bays (e.g., Cariaco, Venezuela (Taylor et al., 2001)), fjords (e.g., Mariager Fjord, Denmark (Zopfi et al., 2001); Saanich Inlet, Canada (Walsh et al., 2009)), and (semi-) enclosed, stratified inland seas (Baltic Sea (Grote et al., 2007), Black Sea (Glaubitz et al., 2010; Jørgensen et al., 1991)). Continental locations include sulfate-rich freshwater environments (e.g., Lake Banyoles, Spain (Noguerola et al., 2015); Lake Cadagno, Switzerland (Camacho et al., 2001)) and even Antarctic meromictic lakes (Lake Vanda, Antarctica (Schutte et al., 2020)). Oxygen deficiency or complete anoxia in deeper water layers either favors the production of hydrogen sulfide during microbial decomposition of organic matter by sulfate-reducing bacteria or intensifies that process so that anoxic zones might expand. In the context of increasing environmental eutrophication and climate change, which is accompanied by rising temperatures and enhanced stratification, the occurrence of oxygen-depleted water zones will expand (Diaz & Rosenberg, 2008; Stramma et al., 2008). This creates the prerequisites for an increased emergence of toxic hydrogen sulfide (Diaz & Rosenberg, 2008). In this regard, it is of particular interest to understand the diverse processes in redoxclines as biogeochemical transition zones and barriers for sulfide diffusion toward upper water layers (Walsh et al., 2009). With this study on the formation of the turbid layer at cenote El Zapote, we add a new aspect to the complex biogeochemistry of redoxclines by showing that chemolithoautotrophic organisms promote authigenic calcite precipitation in an aphotic, pelagic redoxcline via nitrate-dependent oxidation of sulfide. Certainly, we are aware that the expression of genes does not necessarily correlate with a prevailing enzymatic activity. However, as will be discussed in the next paragraphs, the combination of transcription-based and hydrogeochemical data provided coherent proof for the assumption of microbially catalyzed depletion of sulfide, nitrate, carbon dioxide, and oxygen in the redoxcline.

The microbial diversity within the cenote differs significantly between the oxic, nitrate-containing freshwater, the hypoxic/anoxic redoxcline and the anoxic, sulfidic halocline, indicating a vertical microbial stratification. The turbid layer, which overlaps with the redoxcline, is strongly dominated by Proteobacteria. As in the freshwater layer, Thaumarchaeota are the dominant archaeal phylum in the redoxcline (Figure 5). The metagenome and metatranscriptome-based diversity analysis points out that the members of the order Hydrogenophilales are the main key players in the pelagic redoxcline and thus in the turbid layer (Figure 6). The 16S rRNA analysis of the Hydrogenophilales extracted from the amplicon data revealed a sequence similarity of 93.7% to “uncultured Hydrogenophilaceae” and of 92.8% to *Annwoodia aquaesulis* (of the order Nitrosomonadales within the β-Proteobacteria) according to the SILVA and NCBI 16S ribosomal RNA database, respectively. The fact that the identity values are below the 94% identity cutoff indicates that these sulfur oxidizers from the cenote El Zapote may form a new genus within the Hydrogenophilaceae family (Schloss & Handelsman, 2005). Future analyses will provide more detailed information on their phylogenetic assignment and genetic features.

The Hydrogenophilales and unassigned β-Proteobacteria were identified in the metatranscriptome as the dominant sulfur oxidizers. The high transcription of *soxYZ* and *soxXA*, together with the lack of *soxCD* reads, indicates that the oxidation of reduced sulfur species proceeds via elemental sulfur as an intermediate product to regenerate the carrier protein SoxYZ again (Frigaard & Dahl, 2008; Sauvé et al., 2007). Both unassigned β-Proteobacteria and Hydrogenophilales also seem to oxidize sulfide via periplasmic FccAB. Especially the Hydrogenophilales, but also β-Proteobacteria expressed the genes encoding the three cytoplasmic enzymes that are responsible for the complete oxidation of sulfide to sulfate (*dsrAB*, *aprAB*, *sat*; Figure 10). In the context of calcite precipitation, this raises the question whether the main product of their metabolic conversion of sulfide is zero-valent sulfur or rather sulfate. In contrast to the incomplete oxidation of sulfide to zero-valent sulfur that would increase the local pH (Kamp et al., 2006) and promote calcite oversaturation, the production of sulfate may result in acidification and rather counteract calcite precipitation. Based on the hydrogeochemical profile (Figure 2), it becomes evident that sulfate is not the predominant product of sulfide oxidation in the redoxcline as no accumulation or increase in sulfate concentration was detected. A cryptic sulfur cycle that would obscure sulfate production via the immediate reduction by sulfate-reducing organisms seems unlikely so far as *sat* genes were predominantly expressed by Hydrogenophilales and Nitrosomonadales instead of sulfate-reducing bacteria (Figure 10). Above all, the presence of particulate sulfur, which was quantitatively analyzed in this study in redoxcline water filtrates, emphasizes that the incomplete oxidation of sulfide to elemental sulfur prevails. It could be clearly demonstrated that there is an enhanced occurrence of particulate S in the center of the redoxcline, which most likely results from elemental sulfur formation (Figure 3). The emergence of particulate sulfur might be even higher as particles smaller than the filter pore size of 0.22 μm are not covered by the data. Regarding potential electron acceptors for sulfide oxidation, the metatranscriptomic data provide strong evidence that the Hydrogenophilales couple the oxidation of sulfide to a complete reduction of nitrate to dinitrogen. This is corroborated by the converging concentration profiles of sulfide and nitrate, which indicate their simultaneous consumption (Figure 2). If the final main product was elemental sulfur, this would imply that the redoxcline and turbid layer are oxidant-limited concerning nitrate as electron acceptor. The hydrogeochemical data confirm this assumption, as the upward flux of HS^- with about 7.9 * 10^{-4} μmol m^{-2} s^{-1} is more than one order of magnitude higher than the downward fluxes of dissolved oxygen with about 9.1 * 10^{-5} and nitrate with about 3.0 * 10^{-5} μmol m^{-2} s^{-1} (Figure 2). Furthermore, it is very likely that the accumulations of small globules within oblate structures found on the filter material from the redoxcline (Figure 4a, c and g) represent intracellular elemental sulfur. Of note, it was established previously that the link between sulfur oxidation, oxidant availability, and calcite precipitation can even exist in a single bacterium. Yang et al. (2019) could establish for *Achromatium* that the organism oxidizes sulfide under oxidant limitation first to sulfur which is combined with calcite precipitation. If the oxidant availability is high, sulfur is oxidized further to sulfate, which leads to a calcite dissolution due to a pH decrease.

Two reaction equations were established to provide an overview of the stoichiometry and energetic aspects (calculated based on Thauer et al., 1977) of the incomplete (Equation 1) vs. complete nitrate-driven chemolithotrophic oxidation of HS^- (Equation 3). Due to the pH of ~6.9, not only HS^- but also H_2S should be present in the redoxcline; therefore, the same is shown for the oxidation of hydrogen sulfide (Equations 2 and 4).

1. Incomplete oxidation of HS^-/H_2S to S^0

$$5HS^- + 2NO_3^- + 7H^+ \rightarrow 5S^0 + N_2 + 6H_2O \tag{1}$$

$\Delta G^{0\prime}$ = −982 kJ/mol
Per mole nitrate: $\Delta G^{0\prime}$ = −491 kJ/mol

$$5H_2S + 2NO_3^- + 2H^+ \rightarrow 5S^0 + N_2 + 6H_2O \tag{2}$$

2. Complete oxidation of HS^-/H_2S to SO_4^{2-}

$$5HS^- + 8NO_3^- + 3H^+ \rightarrow 5SO_4^{2-} + 4N_2 + 4H_2O \tag{3}$$

$\Delta G^{0\prime}$ = −3,722 kJ/mol
Per mole nitrate: $\Delta G^{0\prime}$ = −465 kJ/mol

$$5H_2S + 8NO_3^- \rightarrow 5SO_4^{2-} + 4N_2 + 4H_2O + 2H^+ \tag{4}$$

Comparing the redox equations 1 and 3, it is evident that the incomplete oxidation of HS^- (Equation 1) leads to a much higher proton consumption, which would contribute to the observed pH shift. Likewise, protons are consumed when H_2S serves as electron donor (Equation 2). However, this does not apply to the complete oxidation of hydrogen sulfide to sulfate (Equation 4) during which protons are produced instead. This supports the assumption that the incomplete oxidation to S^0 is of major significance. Moreover, the incomplete oxidation of HS^- (Equation 1) requires a quarter of the nitrate demand of the complete oxidation to sulfate (Equation 3)—a relevant factor in the electron acceptor-limited redox regime. Furthermore, the aerobic ammonium-oxidizing activity of Thaumarchaeota could lead to a constant nitrite supply that can also be used by microorganisms. At the same time, Thaumarchaeota will deplete the exceedingly limited amount of downwards diffusing oxygen at the top of the redoxcline and create anoxic conditions in its center. This also directs the metabolism of the Hydrogenophilales to nitrate instead of oxygen reduction (Boden et al., 2017).

Incomplete sulfide oxidation can be thermodynamically favorable under electron acceptor-limited conditions. Certainly, the complete oxidation of sulfide to sulfate (Equation 3) coupled to denitrification yields a higher overall Gibbs free energy under standard state conditions compared with the partial oxidation to S^0 (Equation 1). However, when the free energy is normalized to the number of molecules of nitrate as the limiting substrate in this metabolic pathway, then it turns out that the energy yield is slightly higher for the incomplete ($\Delta G^{0'} = -491$ kJ/mol; Equation 1) compared with the complete oxidation of sulfide ($\Delta G^{0'} = -465$ kJ/mol; Equation 3). Nevertheless, in the environmental context the availability of the different substrates and the kinetics of their conversion will be decisive for the dominance of one metabolic routine over the other.

A parallel important process in the redoxcline is mainly conducted by the Hydrogenophilales and unassigned β-Proteobacteria via the Calvin cycle (Figures 7 and 10). Microbial autotrophic depletion of carbon dioxide also favors precipitation of calcite due to a shift in the carbonate balance (Castanier et al., 1999, 2000; Castro-Alonso et al., 2019). In this layer, autotrophic bacteria and archaea strongly depend on the upwards diffusion of carbon dioxide, which is released by bacterial decomposition of organic matter in the sediment of the debris mound in the center of the cenote (Figure 1). The flux of bicarbonate (Figure 2), together with the local accumulation of ^{13}C bicarbonate (Ritter et al., 2019), points to a dominant microbial carbon dioxide assimilation in the redoxcline.

Thaumarchaeota (family Nitrosopumilaceae) were the second most dominant group in the metatranscriptome and stand out by their high expression of *amoA* that is involved in the oxidation of ammonium. At the upper edge of the redoxcline, it is noticeable that oxygen and ammonium, both substrates of Thaumarchaeota, disappear at the same water level (Figure 2). Thaumarchaeota are well adapted to substrate limitations (Könneke et al., 2005; Martens-Habbena et al., 2009; Walker et al., 2010) and have already been identified in other pelagic redoxclines and oxygen minimum zones (Berg et al., 2015; Labrenz et al., 2010; Muck et al., 2019). Like the Hydrogenophilales, Thaumarchaeota may also contribute to the local pH shift, and finally calcite precipitation, by their autotrophic carbon dioxide fixation (Figure 11). They harbor the most efficient aerobic autotrophic CO_2 fixation pathway (3-HP/4-HB) (Könneke et al., 2014). Hence, the lower expression of genes involved in this pathway compared with the Calvin Cycle should not be directly correlated with the fraction by which these organisms contribute to the overall process of carbon dioxide fixation. The 3-HP/4-HB pathway is highly efficient, and lower gene expression might still lead to a significant proportion of Thaumarchaeota-based primary production. Moreover, the Thaumarchaeota will most likely also support the observed denitrification-dependent sulfide oxidation not only be oxygen depletion but also nitrite production.

Combining the hydrogeochemical data with the model of microbial contribution to inorganic calcite precipitation, it can be concluded that the pH (as a result of microbial metabolic activity) is the central controlling factor. Potentially, the pH and SI values are higher on the microscale close to the cells than the ones measured in the redoxcline, but this aspect still needs to be addressed. However, in the water column, it is noticeable that the pH peak is actually situated

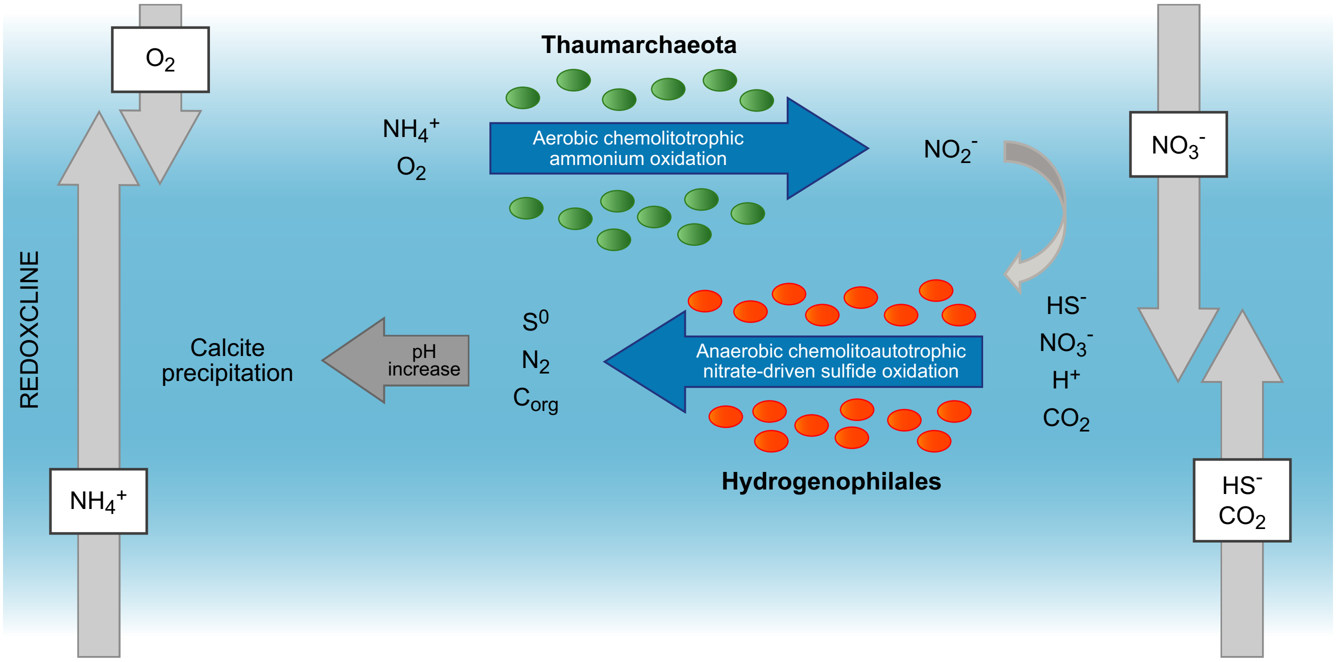

FIGURE 11 Interactions of microbial key players identified in the pelagic redoxcline of cenote El Zapote. Thaumarchaeota thrive in the gradients of oxygen and ammonium at the upper edge of the redoxcline, where minimal concentrations of oxygen seem to be available for the oxidation of ammonium to nitrite. By oxygen depletion, they provide anoxic conditions in the center of the redoxcline, where chemolithoautotrophic Hydrogenophilales conduct anaerobic nitrate-driven sulfide oxidation. Thereby, Hydrogenophilales depend on the upwards diffusion of sulfide and carbon dioxide, as well as the downwards diffusion of the electron acceptors nitrate and nitrite, the product of Thaumarchaeota. Due to oxidant limitations, the oxidation of hydrogen sulfide mainly terminates at the stage of zero-valent sulfur. The simultaneous consumption of sulfide, nitrate, carbon dioxide, and protons results in a pH shift that creates conditions for authigenic calcite precipitation and the formation of the turbid layer in the redoxcline of cenote El Zapote

slightly lower than the measured maximum values of turbidity and the occurrence of particulate sulfur and calcium. The periodic movement of the halocline of the cenote El Zapote as described by Ritter (2020) might be a plausible explanation. Precipitation (rain) builds up the freshwater body of the Yucatán karst aquifer and with it that of the cenote, which leads to a compensatory movement of the underlying water layers downwards and to the sides leading to lowering of the halocline and redoxcline. On the contrary, prolonged periods without precipitation or droughts lead to a thinner freshwater layer and thus to an elevation of the halocline. In addition, the daily tides and general sea-level variations influence the vertical positioning of the halocline (Ritter et al., 2019). As the halocline rises, particles in the redoxcline should also be carried upwards because of the density gradient toward the halocline. Thereby, their specific gravity, which describes the density ratio of two substances, plays a role. Small particles will react and be pushed upwards faster than larger ones, which will most likely be carried along with a time lag. In contrast, heavier particles are expected to sink downwards faster again during the lowering of the halocline. Small particles, however, will move back more slowly (depending on their specific gravity). Those small particles, which have not sunk back to the original initial water level by the time of the next halocline elevation, will be pushed up further during the next elevation. As long as the calcite particles stay in the growth zone around the positive pH peak in the redoxcline, particles will mostly likely keep growing until they reach a certain mass at which they are no longer pushed out of the growth layer. Then, these heavy particles sink into the deeper water zones, where they may dissolve again due to the lower pH in the halocline. In short, the periodic vertical dynamics of the halocline, together with the diversity of particle sizes, may explain the accumulation of small particles and the maximum in turbidity just above the pH peak. Although there are no indications to speculate on controlled biomineralization of calcite by the microorganisms so far, it is interesting to note that calcite biomineralization was previously also discussed as a mechanism to influence microbial motility by gravitaxis as calcite inclusions could considerably increase the cells buoyancy (Monteil et al., 2021).

In this study, nitrate-driven sulfide oxidation (ND-SO) (Bailey et al., 2009; Himmler et al., 2018), combined with autotrophy, was identified as the key biogeochemical process that influences the equilibrium between carbonate dissolution and precipitation. The turbidity in the redoxcline does not only result from the precipitation of calcite but also from the formation of (most likely intracellular) sulfur globules. To our knowledge, neither chemolithoautotrophically induced calcite precipitation in aphotic, pelagic redoxclines nor the specific role of Hydrogenophilales in this context, has been described so far. The identified microbial key processes together with the described oscillatory dynamics of the halocline and thus of the calcite precipitation zone could form the basis for a speleothem growth regulated by the planktonic phase, as proposed by Ritter et al. (2019). Indeed, some features of Hells Bells such as the large size and shape of the dog-tooth calcite crystals suggest such a mechanism. Therefore, further studies will have to address the question how MICCP in the planktonic phase of the turbid layer of the cenote El Zapote is related to the growth of the spectacular Hells Bells in more detail. Since sulfur-oxidizing bacteria are described to play a key role in many other pelagic redoxclines, microbially promoted calcite precipitation may also occur in a similar way in these stratified aquatic systems but has yet to be discovered. In association with environmental changes such as rising temperatures and eutrophication, and thus with the increasing occurrence of sulfide-rich oxygen-depleted water zones, it is even more important to better understand the complex biogeochemical processes occurring in pelagic redoxclines. Future research will show whether MICCP is similarly relevant in other redoxclines.

5 | CONCLUSIONS

With this study on the microbial activity in context of calcite precipitation and thus the formation of the turbid layer in the cenote El Zapote, Mexico, we add a new aspect to the complex biogeochemistry of redoxclines. Based on our metagenomic and metatranscriptomic profiling of the microbiome, it was shown that microorganisms could metabolically promote authigenic calcite precipitation in an aphotic, pelagic redoxcline via chemolithoautotrophic nitrate-dependent oxidation of sulfide. The detected presence and accumulation of particulate zero-valent sulfur in the redoxcline underlined the model that the oxidation is rather incomplete due to electron acceptor limitation resulting in zero-valent sulfur as the predominant metabolic product. The consequent positive pH shift is responsible for calcite oversaturation, precipitation, and finally the growth of calcite particles within the redoxcline. The simultaneous generation of sulfur and calcite particles transforms the water zone overlapping with the redoxcline into a white, cloudy turbid layer and may further be related to the formation of Hells Bells underwater speleothems. Furthermore, microbially induced calcite precipitation as revealed here in cenote El Zapote could potentially play a role in other pelagic redoxclines of stagnant, sulfate-rich waters.

ACKNOWLEDGMENTS

The authors very much appreciated the great support by the owners of Cenote Zapote Ecopark, Rosario Fátima González Alcocer and Santos Zuñiga Roque, and their team members during the fieldwork. We wish to express our thanks to the technical divers Christine Loew and Dirk Penzel for their excellent work during the challenging sampling campaigns at cenote El Zapote. Thank you very much, Jerónimo Avilés, for initiating and pushing the investigation of Hells Bells. Thanks to Vicente Fito and his team for sharing the initial discovery if the Hells Bells at cenote El Zapote in 2009. The authors also acknowledge the impressive photographic material on Hells Bells provided by Valentina Cucchiara (liquidjunglemedia.com). We would like to thank Stefan and Silvia Rheinberger for their excellent support with water analyses and the examination of hydrogeochemical data. This research has been supported by the Deutsche

Forschungsgemeinschaft (grants no. STI128/28 and STI128/36) and the CONACYT-FONCICYT-DADC (grant no. 000000000278227). Open Access funding enabled and organized by Projekt DEAL.

CONFLICT OF INTEREST

The authors declare no competing interests.

DATA AVAILABILITY STATEMENT

The complete hydrogeochemical data sets (from 2018), which are the basis of the water profiles (Figure 2), are available on https://doi.org/10.11588/data/TMYLWS. The raw data from the sampling campaign (in 2020) addressing the quantification of particulate sulfur and calcite together with the respective *in situ* parameters during sampling are available via https://doi.org/10.11588/data/GYLDH5. All 16S rRNA amplicon and metagenomic/metatranscriptomic raw reads included in this study are publicly available through NCBI BioProject PRJNA635010.

ORCID

Kerstin M. Leberecht https://orcid.org/0000-0002-0733-7509
Simon M. Ritter https://orcid.org/0000-0002-1152-8754
Lukas Klose https://orcid.org/0000-0001-7616-4878
Johannes Gescher https://orcid.org/0000-0002-1625-8810

REFERENCES

Addlesee, H. A., & Hunter, C. N. (1999). Physical mapping and functional assignment of the geranylgeranyl-bacteriochlorophyll reductase gene, *bchP*, of *Rhodobacter sphaeroides*. *Journal of Bacteriology*, *181*(23), 7248–7255. https://doi.org/10.1128/JB.181.23.7248-7255.1999

Alvarez, L., Bricio, C., Blesa, A., Hidalgo, A., & Berenguer, J. (2014). Transferable denitrification capability of *Thermus thermophilus*. *Applied and Environmental Microbiology*, *80*(1), 19–28. https://doi.org/10.1128/AEM.02594-13

Bailey, J. V., Orphan, V. J., Joye, S. B., & Corsetti, F. A. (2009). Chemotrophic microbial mats and their potential for preservation in the rock record. *Astrobiology*, *9*(9), 843–859. https://doi.org/10.1089/ast.2008.0314

Berg, C., Vandieken, V., Thamdrup, B., & Jürgens, K. (2015). Significance of archaeal nitrification in hypoxic waters of the Baltic Sea. *The ISME Journal*, *9*(6), 1319–1332. https://doi.org/10.1038/ismej.2014.218

Boden, R., Hutt, L. P., & Rae, A. W. (2017). Reclassification of *Thiobacillus aquaesulis* (Wood & Kelly, 1995) as *Annwoodia aquaesulis* gen. nov., comb. nov., transfer of *Thiobacillus* (Beijerinck, 1904) from the Hydrogenophilales to the Nitrosomonadales, proposal of Hydrogenophilalia class. nov. *International Journal of Systematic and Evolutionary Microbiology*, *67*(5), 1191–1205. https://doi.org/10.1099/ijsem.0.001927

Bolger, A. M., Lohse, M., & Usadel B. (2014). Trimmomatic: a flexible trimmer for Illumina sequence data. *Bioinformatics*, *30*(15), 2114–2120. https://doi.org/10.1093/bioinformatics/btu170

Boughanemi, S., Lyonnet, J., Infossi, P., Bauzan, M., Kosta, A., Lignon, S., Giudici-Orticoni, M. T., & Guiral, M. (2016). Microbial oxidative sulfur metabolism: Biochemical evidence of the membrane-bound heterodisulfide reductase-like complex of the bacterium *Aquifex aeolicus*. *FEMS Microbiology Letters*, *363*(15), fnw156. https://doi.org/10.1093/femsle/fnw156

Bray, N. L., Pimentel, H., Melsted, P., & Pachter, L. (2016). Near-optimal probabilistic RNA-seq quantification. *Nature Biotechnology*, *34*(5), 525–527. https://doi.org/10.1038/nbt.3519

Buchfink, B., Xie, C., & Huson, D. H. (2015). Fast and sensitive protein alignment using DIAMOND. *Nature Methods*, *12*(1), 59–60. https://doi.org/10.1038/nmeth.3176

Camacho, A., Erez, J., Chicote, A., Florín, M., Squires, M. M., Lehmann, C., & Backofen, R. (2001). Microbial microstratification, inorganic carbon photoassimilation and dark carbon fixation at the chemocline of the meromictic Lake Cadagno (Switzerland) and its relevance to the food web. *Aquatic Sciences*, *63*(1), 91–106. https://doi.org/10.1007/PL00001346

Castanier, S., Le Métayer-Levrel, G., & Perthuisot, J.-P. (1999). Ca-carbonates precipitation and limestone genesis - the microbiogeologist point of view. *Sedimentary Geology*, *126*(1–4), 9–23. https://doi.org/10.1016/S0037-0738(99)00028-7

Castanier, S., Le Metayer-Levrel, G., & Perthuisot, J.-P. (2000). Bacterial roles in the precipitation of carbonate minerals. In R. E. Riding, & S. M. Awramik (Eds.), *Microbial sediments* (pp. 32–39). Springer.

Castro-Alonso, M. J., Montañez-Hernandez, L. E., Sanchez-Muñoz, M. A., Macias Franco, M. R., Narayanasamy, R., & Balagurusamy, N. (2019). Microbially induced calcium carbonate precipitation (MICP) and its potential in bioconcrete: microbiological and molecular concepts. *Frontiers in Materials*, *6*, 126. https://doi.org/10.3389/fmats.2019.00126

Chen, Z.-W., Koh, M., Van Driessche, G., Van Beeumen, J. J., Bartsch, R. G., Meyer, T. E., Cusanovich, M. A., & Mathews, F. S. (1994). The structure of flavocytochrome c sulfide dehydrogenase from a purple phototrophic bacterium. *Science*, *266*(5184), 430–432. https://doi.org/10.1126/science.7939681

Diaz, R. J., & Rosenberg, R. (2008). August). Spreading dead zones and consequences for marine ecosystems. *Science*, *321*, 926–929. https://doi.org/10.1126/science.1156401

Dupraz, C., Reid, R. P., Braissant, O., Decho, A. W., Norman, R. S., & Visscher, P. T. (2009). Processes of carbonate precipitation in modern microbial mats. *Earth-Science Reviews*, *96*(3), 141–162. https://doi.org/10.1016/j.earscirev.2008.10.005

Frigaard, N.-U., & Dahl, C. (2008). Sulfur metabolism in phototrophic sulfur bacteria. In R. Poole (Ed.), *Advances in microbial physiology* (vol. *54*, pp. 103–200). Academic Press. https://doi.org/10.1016/S0065-2911(08)00002-7

Fromme, P. (1996). Structure and function of photosystem I. *Current Opinion in Structural Biology*, *6*(4), 473–484. https://doi.org/10.1016/S0959-440X(96)80112-6

Glaubitz, S., Labrenz, M., Jost, G., & Jürgens, K. (2010). Diversity of active chemolithoautotrophic prokaryotes in the sulfidic zone of a Black Sea pelagic redoxcline as determined by rRNA-based stable isotope probing. *FEMS Microbiology Ecology*, *74*(1), 32–41. https://doi.org/10.1111/j.1574-6941.2010.00944.x

Görgen, S., Benzerara, K., Skouri-Panet, F., Gugger, M., Chauvat, F., & Cassier-Chauvat, C. (2020). The diversity of molecular mechanisms of carbonate biomineralization by bacteria. *Discover Materials*, *1*(1), 2. https://doi.org/10.1007/s43939-020-00001-9

Grabarczyk, D. B., & Berks, B. C. (2017). Intermediates in the Sox sulfur oxidation pathway are bound to a sulfane conjugate of the carrier protein SoxYZ. *PLoS One*, *12*(3), e0173395. https://doi.org/10.1371/journal.pone.0173395

Griesbeck, C., Schütz, M., Schödl, T., Bathe, S., Nausch, L., Mederer, N., Vielreicher, M., & Hauska, G. (2002). Mechanism of sulfide-quinone reductase investigated using site-directed mutagenesis and sulfur analysis. *Biochemistry*, *41*(39), 11552–11565. https://doi.org/10.1021/bi026032b

Grote, J., Labrenz, M., Pfeiffer, B., Jost, G., & Jürgens, K. (2007). Quantitative distributions of Epsilonproteobacteria and a *Sulfurimonas* subgroup in pelagic redoxclines of the central Baltic Sea. *Applied and Environmental Microbiology*, *73*(22), 7155–7161. https://doi.org/10.1128/AEM.00466-07

Gruber-Vodicka, H. R., Seah, B. K. B., & Pruesse, E. (2020). phyloFlash: Rapid small-subunit rRNA profiling and targeted assembly from metagenomes. *mSystems*, *5*(5). https://doi.org/10.1128/msystems.00920-20

Himmler, T., Smrzka, D., Zwicker, J., Kasten, S., Shapiro, R. S., Bohrmann, G., & Peckmann, J. (2018). Stromatolites below the photic zone in the northern Arabian Sea formed by calcifying chemotrophic microbial mats. *Geology*, *46*(4), 339–342. https://doi.org/10.1130/G39890.1

Huerta-Cepas, J., Forslund, K., Coelho, L. P., Szklarczyk, D., Jensen, L. J., von Mering, C., & Bork, P. (2017). Fast Genome-Wide Functional Annotation through Orthology Assignment by eggNOG-Mapper. *Molecular Biology and Evolution*, *34*(8), 2115–2122. https://doi.org/10.1093/molbev/msx148

Huerta-Cepas, J., Szklarczyk, D., Heller, D., Hernández-Plaza, A., Forslund, S. K., Cook, H., Mende, D. R., Letunic, I., Rattei, T., Jensen, L. J., von Mering, C., & Bork, P. (2019). eggNOG 5.0: a hierarchical, functionally and phylogenetically annotated orthology resource based on 5090 organisms and 2502 viruses. *Nucleic Acids Research*, *47*(D1), D309–D314. https://doi.org/10.1093/nar/gky1085

Huggett, R. (2003). Karst landscapes. In *Fundamentals of geomorphology (Routledge fundamentals of physical geography)* (pp. 386). Routledge.

Hyatt, D., Chen, G.-L., LoCascio, P. F., Land, M. L., Larimer, F. W., & Hauser, L. J. (2010). Prodigal: prokaryotic gene recognition and translation initiation site identification. *BMC Bioinformatics*, *11*(1). https://doi.org/10.1186/1471-2105-11-119

Imhoff, J. F. (2016). New dimensions in microbial ecology-functional genes in studies to unravel the biodiversity and role of functional microbial groups in the environment. *Microorganisms*, *4*(2), 19. https://doi.org/10.3390/microorganisms4020019

Jørgensen, B. B., Fossing, H., Wirsen, C. O., & Jannasch, H. W. (1991). Sulfide oxidation in the anoxic Black Sea chemocline. *Deep Sea Research Part A. Oceanographic Research Papers*, *38*, S1083–S1103. https://doi.org/10.1016/S0198-0149(10)80025-1

Jorgensen, B. B., Kuenen, J. G., & Cohen, Y. (1979). Microbial transformations of sulfur compounds in a stratified lake (Solar Lake, Sinai). *Limnology and Oceanography*, *24*(5), 799–822. https://doi.org/10.4319/lo.1979.24.5.0799

Kamp, A., Stief, P., & Schulz-Vogt, H. N. (2006). Anaerobic sulfide oxidation with nitrate by a freshwater *Beggiatoa* enrichment culture. *Applied and Environmental Microbiology*, *72*(7), 4755–4760. https://doi.org/10.1128/AEM.00163-06

Kang, D. D., Li, F., Kirton, E., Thomas, A., Egan, R., An, H., & Wang, Z. (2019). MetaBAT 2: An adaptive binning algorithm for robust and efficient genome reconstruction from metagenome assemblies. *PeerJ*, *7*, e7359. https://doi.org/10.7717/peerj.7359

Klindworth, A., Pruesse, E., Schweer, T., Peplies, J., Quast, C., Horn, M., & Glöckner, F. O. (2013). Evaluation of general 16S ribosomal RNA gene PCR primers for classical and next-generation sequencing-based diversity studies. *Nucleic Acids Research*, *41*(1), 1–11. https://doi.org/10.1093/nar/gks808

Koch, T., & Dahl, C. (2018). A novel bacterial sulfur oxidation pathway provides a new link between the cycles of organic and inorganic sulfur compounds. *The ISME Journal*, *12*(10), 2479–2491. https://doi.org/10.1038/s41396-018-0209-7

Könneke, M., Bernhard, A. E., De La Torre, J. R., Walker, C. B., Waterbury, J. B., & Stahl, D. A. (2005). Isolation of an autotrophic ammonia-oxidizing marine archaeon. *Nature*, *437*(7058), 543–546. https://doi.org/10.1038/nature03911

Könneke, M., Schubert, D. M., Brown, P. C., Hügler, M., Standfest, S., Schwander, T., Schada von Borzyskowski, L., Erb, T. J., Stahl, D. A. & Berg, I. A. (2014). Ammonia-oxidizing archaea use the most energy-efficient aerobic pathway for CO_2 fixation. *Proceedings of the National Academy of Sciences of the United States of America*, *111*(22), 8239–8244. https://doi.org/10.1073/pnas.1402028111

Kovacs, S. E., Reinhardt, E. G., Chatters, J. C., Rissolo, D., Schwarcz, H. P., Collins, S. V., Kim, S.-T., Nava Blank, A., & Luna Erreguerena, P. (2017). Calcite raft geochemistry as a hydrological proxy for Holocene aquifer conditions in Hoyo Negro and Ich Balam (Sac Actun Cave System), Quintana Roo, Mexico. *Quaternary Science Reviews*, *175*, 97–111. https://doi.org/10.1016/j.quascirev.2017.09.006

Labrenz, M., Sintes, E., Toetzke, F., Zumsteg, A., Herndl, G. J., Seidler, M., & Jürgens, K. (2010). Relevance of a crenarchaeotal subcluster related to *Candidatus* Nitrosopumilus maritimus to ammonia oxidation in the suboxic zone of the central Baltic Sea. *The ISME Journal*, *4*(12), 1496–1508. https://doi.org/10.1038/ismej.2010.78

Langmead, B., & Salzberg, S. L. (2012). Fast gapped-read alignment with Bowtie 2. *Nature Methods*, *9*(4), 357–359. https://doi.org/10.1038/nmeth.1923

Li, D., Liu, C.-M., Luo R., Sadakane K., & Lam T.-W. (2015). MEGAHIT: an ultra-fast single-node solution for large and complex metagenomics assembly via succinct de Bruijn graph. *Bioinformatics*, *31*(10), 1674–1676. https://doi.org/10.1093/bioinformatics/btv033

Li, D., Luo, R., Liu, C.-M., Leung, C.-M., Ting, H.-F., Sadakane, K., Yamashita, H., & Lam, T.-W. (2016). MEGAHIT v1.0: A fast and scalable metagenome assembler driven by advanced methodologies and community practices. *Methods*, *102*, 3–11. https://doi.org/10.1016/j.ymeth.2016.02.020

Löffler, M., Feldhues, J., Venceslau, S. S., Kammler, L., Grein, F., Pereira, I. A. C., & Dahl, C. (2020). DsrL mediates electron transfer between NADH and rDsrAB in *Allochromatium vinosum*. *Environmental Microbiology*, *22*(2), 783–795. https://doi.org/10.1111/1462-2920.14899

López-Martínez, R., Gázquez, F., Calaforra, J., Audra, P., Bigot, J., Pi Puig, T., Alcántara-Hernández, R., Navarro, Á., Crochet, P., Corona Martínez, L., & Daza Brunet, R. (2020). Bubble trail and folia in cenote Zapote, Mexico: Petrographic evidence for abiotic precipitation driven by CO_2 degassing below the water table. *International Journal of Speleology*, *49*(3), 173–186. https://doi.org/10.5038/1827-806X.49.3.2344

Marcia, M., Ermler, U., Peng, G., & Michel, H. (2009). The structure of *Aquifex aeolicus* sulfide: Quinone oxidoreductase, a basis to understand sulfide detoxification and respiration. *Proceedings of the National Academy of Sciences of the United States of America*, *106*(24), 9625–9630. https://doi.org/10.1073/pnas.0904165106

Martens-Habbena, W., Berube, P. M., Urakawa, H., De La Torre, J. R., & Stahl, D. A. (2009). Ammonia oxidation kinetics determine niche separation of nitrifying Archaea and Bacteria. *Nature*, *461*(7266), 976–979. https://doi.org/10.1038/nature08465

Monteil, C. L., Benzerara, K., Menguy, N., Bidaud, C. C., Michot-Achdjian, E., Bolzoni, R., Mathon, F. P., Coutaud, M., Alonso, B., Garau, C., Jézéquel, D., Viollier, E., Ginet, N., Floriani, M., Swaraj, S., Sachse, M., Busigny, V., Duprat, E., Guyot, F., & Lefevre, C. T. (2021). Intracellular amorphous Ca-carbonate and magnetite biomineralization by a magnetotactic bacterium affiliated to the Alphaproteobacteria. *The ISME Journal*, *15*(1), 1–18. https://doi.org/10.1038/s41396-020-00747-3

Muck, S., De Corte, D., Clifford, E. L., Bayer, B., Herndl, G. J., & Sintes, E. (2019). Niche differentiation of aerobic and anaerobic ammonia oxidizers in a high latitude deep oxygen minimum zone. *Frontiers in Microbiology*, *10*, 2141. https://doi.org/10.3389/fmicb.2019.02141

Müller, A. L., Kjeldsen, K. U., Rattei, T., Pester, M., & Loy, A. (2015). Phylogenetic and environmental diversity of DsrAB-type dissimilatory (bi)sulfite reductases. *The ISME Journal*, *9*(5), 1152–1165. https://doi.org/10.1038/ismej.2014.208

Mulo, P., Sicora, C., & Aro, E.-M. (2009). Cyanobacterial *psbA* gene family: Optimization of oxygenic photosynthesis. *Cellular and Molecular Life Sciences*, *66*(23), 3697–3710. https://doi.org/10.1007/s00018-009-0103-6

Nims, C., Cron, B., Wetherington, M., Macalady, J., & Cosmidis, J. (2019). Low frequency Raman Spectroscopy for micron-scale and in vivo characterization of elemental sulfur in microbial samples. *Scientific Reports*, *9*(1), 7971. https://doi.org/10.1038/s41598-019-44353-6

Noguerola, I., Picazo, A., Llirós, M., Camacho, A., & Borrego, C. M. (2015). Diversity of freshwater *Epsilonproteobacteria* and dark inorganic carbon fixation in the sulphidic redoxcline of a meromictic karstic lake. *FEMS Microbiology Ecology*, *91*(7), fiv086. https://doi.org/10.1093/femsec/fiv086

Oh-oka, H., & Blankenship, R. E. (2004). Green bacteria: Secondary electron donor (Cytochromes). In W. J. Lennarz, & M. Lane (Eds.), *Encyclopedia of biological chemistry* (pp. 321–324). Elsevier.

Parks, D. H., Imelfort, M., Skennerton, C. T., Hugenholtz, P., & Tyson, G. W. (2015). CheckM: Assessing the quality of microbial genomes recovered from isolates, single cells, and metagenomes. *Genome Research*, *25*(7), 1043–1055. https://doi.org/10.1101/gr.186072.114

Parkhurst, D. L., & Appelo, C. A. J. (1999). User's guide to PHREEQC (Version 2): A computer program for speciation, batch-reaction, one-Dimensional transport, and inverse geochemical calculations. *Water-Resources Investigations Report*, *99*(4259).

Reinartz, M., Tschäpe, J., Brüser, T., Trüper, H. G., & Dahl, C. (1998). Sulfide oxidation in the phototrophic sulfur bacterium *Chromatium vinosum*. *Archives of Microbiology*, *170*(1), 59–68. https://doi.org/10.1007/s002030050615

Ritter, S. M. (2020). *Unravelling the formation of Hells Bells: underwater speleothems from the Yucatán Peninsula in Mexico*. (Doctoral dissertation, Heidelberg University). https://doi.org/10.11588/heidok.00027813

Ritter, S. M., Isenbeck-Schröter, M., Scholz, C., Keppler, F., Gescher, J., Klose, L., Schorndorf, N., Avilés Olguín, J., González-González, A., Stinnesbeck, W. (2019). Subaqueous speleothems (Hells Bells) formed by the interplay of pelagic redoxcline biogeochemistry and specific hydraulic conditions in the El Zapote sinkhole, Yucatán Peninsula, Mexico. *Biogeosciences*, *16*(11), 2285–2305. https://doi.org/10.5194/bg-16-2285-2019

Rodionov, D. A., Dubchak, I. L., Arkin, A. P., Alm, E. J., & Gelfand, M. S. (2005). Dissimilatory metabolism of nitrogen oxides in bacteria: Comparative reconstruction of transcriptional networks. *PLoS Computational Biology*, *1*(5), e55. https://doi.org/10.1371/journal.pcbi.0010055

Rother, D., Henrich, H. J., Quentmeier, A., Bardischewsky, F., & Friedrich, C. G. (2001). Novel genes of the *sox* gene cluster, mutagenesis of the flavoprotein SoxF, and evidence for a general sulfur-oxidizing system in *Paracoccus pantotrophus* GB17. *Journal of Bacteriology*, *183*(15), 4499–4508. https://doi.org/10.1128/JB.183.15.4499-4508.2001

Sauvé, V., Bruno, S., Berks, B. C., & Hemmings, A. M. (2007). The SoxYZ complex carries sulfur cycle intermediates on a peptide swinging arm. *Journal of Biological Chemistry*, *282*(32), 23194–23204. https://doi.org/10.1074/jbc.M701602200

Schloss, P. D., & Handelsman, J. (2005). Introducing DOTUR, a computer program for defining operational taxonomic units and estimating species richness. *Applied and Environmental Microbiology*, *71*(3), 1501–1506. https://doi.org/10.1128/AEM.71.3.1501-1506.2005

Schutte, C. A., Samarkin, V. A., Peters, B., Madigan, M. T., Bowles, M., Morgan-Kiss, R., Casciotti, K., & Joye, S. (2020). Vertical stratification and stability of biogeochemical processes in the deep saline waters of Lake Vanda, Antarctica. *Limnology and Oceanography*, *65*(3), 569–581. https://doi.org/10.1002/lno.11327

Shi, T., Bibby, T. S., Jiang, L., Irwin, A. J., & Falkowski, P. G. (2005). Protein interactions limit the rate of evolution of photosynthetic genes in cyanobacteria. *Molecular Biology and Evolution*, *22*(11), 2179–2189. https://doi.org/10.1093/molbev/msi216

Stahl, D. A., & Amann, R. (1991). Development and application of nucleic acid probes. *Nucleic acid techniques in bacterial systematics*, 205–248.

Stinnesbeck, W., Frey, E., Zell, P., Avilés, J., Hering, F., Frank, N., Arps, J., Geenen, A., Gescher, J., Isenbeck-Schröter, M., Ritter, S., Stinnesbeck, S., Núñez, E. A., Dahne, V. F., González, A. G., & Deininger, M. (2018). Hells Bells – Unique speleothems from the Yucatán Peninsula, Mexico, generated under highly specific subaquatic conditions. *Palaeogeography, Palaeoclimatology, Palaeoecology*, *489*, 209–229. https://doi.org/10.1016/j.palaeo.2017.10.012

Stockdreher, Y., Sturm, M., Josten, M., Sahl, H.-G., Dobler, N., Zigann, R., & Dahl, C. (2014). New proteins involved in sulfur trafficking in the cytoplasm of *Allochromatium vinosum*. *The Journal of Biological Chemistry*, *289*(18), 12390–12403. https://doi.org/10.1074/jbc.M113.536425

Stramma, L., Johnson, G. C., Sprintall, J., & Mohrholz, V. (2008). Expanding oxygen-minimum zones in the tropical oceans. *Science*, *320*(5876), 655–658. https://doi.org/10.1126/science.1153847

Tanabe, T. S., Leimkühler, S., & Dahl, C. (2019). Chapter Seven - The functional diversity of the prokaryotic sulfur carrier protein TusA. In R. Poole (Ed.), *Advances in microbial physiology* (vol. *75*, pp. 233–277). Academic Press.

Taylor, G. T., Iabichella, M., Ho, T.-Y., Scranton, M. I., Thunell, R. C., Muller-Karger, F., & Varela, R. (2001). Chemoautotrophy in the redox transition zone of the Cariaco Basin: A significant midwater source of organic carbon production. *Limnology and Oceanography*, *46*(1), 148–163. https://doi.org/10.4319/lo.2001.46.1.0148

Thauer, R. K., Jungermann, K., & Decker, K. (1977). Energy conservation in chemotrophic anaerobic bacteria. *Bacteriological Reviews*, *41*(1), 100–180. https://doi.org/10.1128/br.41.1.100-180.1977

Walker, C. B., De La Torre, J. R., Klotz, M. G., Urakawa, H., Pinel, N., Arp, D. J., Brochier-Armanet, C., Chain, P. S., Chan, P. P., Gollabgir, A., Hemp, J., Hügler, M., Karr, E. A., Könneke, M., Shin, M., Lawton, T. J., Lowe, T., Martens-Habbena, W., Sayavedra-Soto, L. A., Lang, D., Sievert, S. M., Rosenzweig, A. C., Manning, G., & Stahl, D. A. (2010). *Nitrosopumilus maritimus* genome reveals unique mechanisms for nitrification and autotrophy in globally distributed marine crenarchaea. *Proceedings of the National Academy of Sciences of the United States of America*, *107*(19), 8818–8823. https://doi.org/10.1073/pnas.0913533107

Walsh, D. A., Zaikova, E., Howes, C. G., Song, Y. C., Wright, J. J., Tringe, S. G., Tortell, P. D., & Hallam, S. J. (2009). Metagenome of a versatile chemolithoautotroph from expanding oceanic dead zones. *Science*, *326*(5952), 578–582. https://doi.org/10.1126/science.1175309

Yang, T., Teske, A., Ambrose, W., Salman-Carvalho, V., Bagnell, R., & Nielsen, L. P. (2019). Intracellular calcite and sulfur dynamics of *Achromatium* cells observed in a lab-based enrichment and aerobic incubation experiment. *Antonie van Leeuwenhoek*, *112*(2), 263–274. https://doi.org/10.1007/s10482-018-1153-2

Zopfi, J., Ferdelman, T. G., Jørgensen, B. B., Teske, A., & Thamdrup, B. (2001). Influence of water column dynamics on sulfide oxidation and other major biogeochemical processes in the chemocline of Mariager Fjord (Denmark). *Marine Chemistry*, *74*(1), 29–51. https://doi.org/10.1016/S0304-4203(00)00091-8

SUPPORTING INFORMATION

Additional supporting information may be found in the online version of the article at the publisher's website.

How to cite this article: Leberecht, K. M., Ritter, S. M., Lapp, C. J., Klose, L., Eschenröder, J., Scholz, C., Kühnel, S., Stinnesbeck, W., Kletzin, A., Isenbeck-Schröter, M., & Gescher, J. (2022). Microbially promoted calcite precipitation in the pelagic redoxcline: Elucidating the formation of the turbid layer. *Geobiology*, *20*, 498–517. https://doi.org/10.1111/gbi.12492